CO_2 Capture by Absorption with Potassium Carbonate
Fourth Quarterly Report 2005

Quarterly Progress Report
Reporting Period Start Date: October 1, 2005
Reporting Period End Date: December 31, 2005
Authors: Gary T. Rochelle, Marcus Hilliard, Eric Chen, Babatunde Oyenekan, Ross Dugas, John McLees, Andrew Sexton, Amorvadee Veawab

January 26, 2005
DOE Award #: DE-FC26-02NT41440
Department of Chemical Engineering
The University of Texas at Austin

Disclaimer

Abstract

The objective of this work is to improve the process for CO_2 capture by alkanolamine absorption/stripping by developing an alternative solvent, aqueous K_2CO_3 promoted by piperazine. In Campaign 3 of the pilot plant, the overall mass transfer coefficient for the stripper with 7 m MEA decreased from 0.06 to 0.01 mol/(m^3.s.kPa) as the rich loading increased from 0.45 to 0.6 mol CO_2/ mol MEA. Anion chromatography has demonstrated that nitrate and nitrite are major degradation products of MEA and PZ with pure oxygen. In measurements with the high temperature FTIR in 7 m MEA the MEA vapor pressure varied from 2 to 20 Pa at 35 to 70^{o}C. In 2.5 m PZ the PZ vapor pressure varied from 0.2 to 1 Pa from 37 to 70^{o}C.

Contents

List of Figures

List of Tables

Introduction

The objective of this work is to improve the process for CO_2 capture by alkanolamine absorption/stripping by developing an alternative solvent, aqueous K_2CO_3 promoted by piperazine. This work expands on parallel bench-scale work with system modeling and pilot plant measurements to demonstrate and quantify the solvent process concepts.

Gary Rochelle is supervising the bench-scale and modeling work; Frank Seibert is supervising the pilot plant. Three graduate students (Babatunde Oyenekan, Ross Dugas, John McLees) have received support during this quarter for direct effort on the scope of this contract. Three students supported by other funding have made contributions this quarter to the scope of this project (Eric Chen – EPA Star Fellowship; Marcus Hilliard, Andrew Sexton – Industrial Associates). Subcontract work was performed at the University of Regina under the supervision of Amy Veawab.

Experimental

Subtask 1.10 describes methods for measuring ionic conductivity, density, and pH of loaded MEA/PZ solutions.

Subtask 2.6 describes measurements of density and pH and a new IC method for solution analysis.

Subtask 3.1 presents methods for analyzing amine degradation products by anion chromatography.

Results and Discussion

Progress has been made on seven subtasks in this quarter:

Subtask 1.8 – Predict Flowsheet Options

The model in Aspen Custom Modeler was used to model vacuum and split product configurations with optimized lean loading. A number of flowsheet options are presented to be used with a vacuum stripper.

Subtask 1.10 – Simulate MEA Baseline

Data obtained from the MEA baseline campaign was further analyzed to characterize absorber temperature profiles and stripper mass transfer. Ionic conductivity, pH, and density were measured for 7 m MEA/2 m piperazine as a function of temperature and CO_2 loading.

Subtask 2.6 – Campaign 4

The test plan for Campaign 4 in the pilot plant includes runs with 5 m K^+/2.5m PZ with the stripper at 1.6 atm and runs with 6.4 m K^+/1.6 m PZ. The pH of these solutions is a moderate function of loading, so pH will be used as a control point in Campaign 4. The new method for measuring piperazine and potassium by cation chromatography produces results from diluted samples in about 5 minutes. The modifications for Campaign 4 include a new cross-exchanger, a system for steam injection into the gas, and a carbon filter.

Subtask 3.1 – Analysis of Degradation Products

Liquid samples have been analyzed from four experiments with MEA and PZ in the degradation apparatus with low gas flow. Acetate, formate, oxalate, nitrite, and nitrate were determined by anion chromatography. The method for determining CO_2 concentration in the solvent has been updated and documented.

Subtask 3.4 – Amine Volatility

Accurate measurements of water vapor pressure have been made in the new bench-scale apparatus with the high temperature gas FTIR. Amine volatility has been measured at 35 to 70^{o}C in unloaded solutions of 7 m MEA and 2.5 m PZ.

Task 5 – Corrosion

A review has been completed on the literature on corrosion in the hot potassium carbonate process.

Conclusions

1. With 7 m MEA in Campaign 3, the maximum temperature bulge in the absorber varied from 3 to 90^{o}F. The bulge was near the top with L/G less than 5 and near the bottom with L/G greater than 6.

2. The overall mass transfer coefficient for the stripper with 7 m MEA decreased from 0.06 to 0.01 mol/(m^3.s.kPa) as the rich loading increased from 0.45 to 0.6 mol CO_2/ mol MEA.

3. With an optimized lean loading the split product configuration is less attractive than simple vacuum stripping with 5 m K^+/2.5 m PZ.

4. In 7 m MEA the MEA vapor pressure varied from 2 to 20 Pa at 35 to 70^{o}C. In 2.5 m PZ the PZ vapor pressure varies from 0.2 to 1 Pa from 37 to 70^{o}C.

5. Nitrate and nitrite are major degradation products of MEA and PZ with pure oxygen. With 7 m MEA the production rate of nitrate/nitrite was 0.25-0.47 mM/hr compared to 0.6-1.0 mM/hr of organic acids. With 2.5 m PZ the production rate of nitrate/nitrite was 0.25 mM/hr compared to only 0.05 mM/hr of organic acids.

6. In 7 m MEA/2 m PZ at 45^{o}C, as the loading increases from 0.1 to 0.56 mol/equiv amine, the pH decreases from 10.3 to 8.3 and the ionic conductivity increases from 13 to 30 mS/cm.

7. Vanadium^{+5} is an effective corrosion inhibitor in hot potassium carbonate/bicarbonate systems. It probably passivates the carbon steel surface by maintaining Fe^{+3} at the surface with conversion of V^{+5} to V^{+4}.

Future Work

We expect the following accomplishments in the next quarter:

Subtask 1.1 – Modify Vapor-Liquid Equilibrium (VLE) Model

A new experimental system will be set up to measure CO_2 VLE with the hot gas FTIR.

Subtask 1.5 – Simulate Base Case Pilot

The absorber data from Campaigns 1 and 2 will be simulated with the spreadsheet model.

Subtask 1.8 – Predict Flowsheet Options

The ACM stripper model will be further modified to simulate rates in the stripper. It will then be used for more accurate simulation of the alternative stripper configurations.

Subtask 1.10 – Simulate MEA Baseline

A master's thesis will completed to fully document the baseline MEA campaign.

Subtask 2.6 – Pilot Plant Campaign 4, Optimization of System Parameters

The testing for Campaign 4 will take place in January 2006.

Subtask 3.1 – Analysis of Degradation Products

Cation chromatography will be further developed to determine ethylenediamine in degraded samples of piperazine.

Subtask 3.4 – Amine Volatility

Piperazine volatility will be measured by the FTIR in the last pilot plant campaign.

Task 1 – Modeling Performance of Absorption/Stripping of CO_2 with Aqueous K_2CO_3 Promoted by Piperazine

Subtask 1.8a – Predict Flowsheet Options – Spreadsheet modeling

By Gary Rochelle

(Supported by the University academic budget)

Vacuum stripping can be considered at a number of operating conditions with progressively lower stripper reboiler T as outlined in Table 1. Because the effective work of the stripper steam is given approximately by $W_{eq} = Q_{stm} \frac{T_{stm} - T_{amb}}{T_{stm}}$, the energy loss associated with the stripper heat duty will decrease systematically until the condensing steam temperature is T_{amb}. If T_{amb} is taken as the condensing temperature of the steam from the low pressure turbine, then such "waste" heat would be available to the system at no cost. Table 1 assumes that the low pressure steam condenses at 40°C with cooling water heated to 35°C.

As the temperature of the reboiler decreases the cost of energy will also be increasingly reduced by the use of various sources of waste heat. Flue gas is typically available at 150°C and could provide heat within 10 to 20°C of the reboiler T. The intercoolers on the CO_2 compressor will have sensible heat available at 175°C. More heat will be available after the first stage compressor if water vapor is left in the gas.

Therefore, even though successively lower reboiler T will require lower stripper P and therefore more compression energy for the CO_2, the total equivalent work for these configurations may decrease with reboiler T.

The primary disadvantage of a lower reboiler T will be the capital cost of the compressor, which will increase with lower suction pressure, not so much because of the increased horsepower, but rather because of the increased gas volume.

All of the configurations given in Table 1 may be enhanced by other features such as split feed and split product.

Table 1. Conditions for Vacuum Stripping.

Configuration	Reboiler T (°C)	Steam T (°C)	Overhead T (°C)	Absorber T (°C)
Simple	70	75	55	40
Simple	55	60	40	40
Multipressure	45	50	40	40
Multipressure	35	40	30	35-40
Simple	35	40	20	25-40

No compression of water vapor

With a reboiler at 70°C in a simple stripper, the overhead vapor will leave at about 55°C. That permits the use of cooling water to condense most of the water vapor in the overhead, so that the compressor sees a vacuum gas which is primarily just the CO_2 product. This vacuum

configuration minimizes the size and horsepower of the compressor. It must use extraction steam and can make use of waste heat above 75°C.

Vapor Recompression

With a reboiler at 55°C in a simple stripper, the rich feed does not have to be heated to avoid flashing at the overhead of about 40°C. The hot lean solution might still be exchanged with a split feed to provide better heat recovery. In this case the overhead water vapor must be compressed in the first stage with the CO_2. The intercooler after the first stage will therefore provide more heat that can be recovered for the 55°C reboiler. Therefore this system would be using vapor recompression for some of the reboiler heat duty. Stripper steam and waste heat would need to be provided at 60°C to provide adequate driving force in the reboiler. The equivalent work of the reboiler will decrease because of the heat recovery and because of the reduced T of the reboiler steam.

Multipressure with no heat exchange

With a multipressure stripper, multiple rich and semi-rich stripper feeds at 40°C can be provided with no heat exchange. The stripper bottoms and the bottom of individual sections of the stripper could be operated at 45°C, so that heat recovery from the hot lean solution is no longer desirable. Stripper steam and waste heat would need to be provided at 50°C. There would be water vapor compressed in all of the stages within the stripper and in the stage leaving the stripper. It might be possible to effectively flash a semirich feed from the temperature bulge of the absorber to recover much of the heat of absorption as stripping steam. Heat could also be recovered by other means from the hot middle of the absorber, such as a recirculating water loop using direct contact.

Free waste heat with multipressure

With a multipressure stripper using a 35°C reboiler, the heat is essentially free as it can use the low pressure steam condensing at 40°C. Since the overhead will be at 30C, absorber rich feed at 35°C will flash and load the compressor with more water vapor. An appropriate recycle of rich and semirich feeds could effectively permit operation of the absorber at 35°C. The heat of CO_2 absorption and other heat in the flue gas can be recovered by solvent recycle or by a water recycle loop to provide much of the heat for the stripper. At these conditions there will be more than enough free heat, the energy cost will all be work required to compress the CO_2 and resulting water vapor.

Refrigerated absorber

A probable limiting case is a 35°C reboiler with a simple stripper. There overhead T would be about 20°C, allowing total heat recovery from the absorber with resulting refrigeration of the absorber to 25-30°C. The lower absorber T would reduce the amount of water vapor showing up at the stripper, but the CO_2 must now be compressed from a very low pressure.

Subtask 1.8b – Predict Flowsheet Options – Aspen Custom Modeler for Stripper

by Babatunde Oyenekan

(Supported by this contract)

Introduction

We have continued to develop the stripper submodel in Aspen Custom Modeler for the overall model of CO_2 absorption/stripping for 7m monoethanolamine (MEA), 5m K^+ / 2.5m PZ and some generic solvents. Previous work suggests that with generic solvents, the optimum ΔH is a function of the stripper configuration used. The vacuum stripper is favored for solvents with $\Delta H_{des} \leq 21$ kcal/gmol CO_2. Since the 5m K^+/2.5m PZ has a lower heat of desorption than 21 kcal/gmol CO_2, the vacuum stripper will be attractive for the solvent. There may be some process configurations that may be quite attractive for the 5m K^+/2.5m PZ solvent. A new process configuration, split product, was evaluated and the results obtained were compared to the vacuum stripper at a 5^{o}C approach. This model divides the stripper into sections with Murphree efficiencies assigned to CO_2, water and temperature. A three-parameter expression approximates the equilibrium behavior of the generic solvents. The results show that the vacuum stripper performs better than the split product configuration. A rate-based model is being developed to predict operation of real columns.

Experimental (Model Formulation)

Stripper Configurations

Vacuum Stripper

The stripper is operated at 30 kPa and the reboiler runs at 60-80^{o}C. The CO_2 is compressed in five intercooled stages to 1000 kPa.

Vacuum stripping has the following features:

1. Lower temperature (less valuable) steam is used to run the reboiler so more electricity can be extracted before the steam is used in the stripper.
2. Additional compression is required for the CO_2.
3. The mass transfer is not as fast as that of the simple stripper because the lower temperature results in slower kinetics.

Vacuum Split Product Stripper

In this configuration (Figure 1), the stripper is run at 30 kPa and the reboiler runs at 60-80^{o}C. The CO_2 is compressed in five intercooled stages to 1000 kPa. The stripper has two feed streams, a rich stream at the top of the stripper, and a semi-lean stream introduced mid-way in the stripper. This stream is taken from an appropriate point in the absorber. The rich and semi-lean streams are cross-exchanged to the maximum extent possible before being introduced into the stripper.

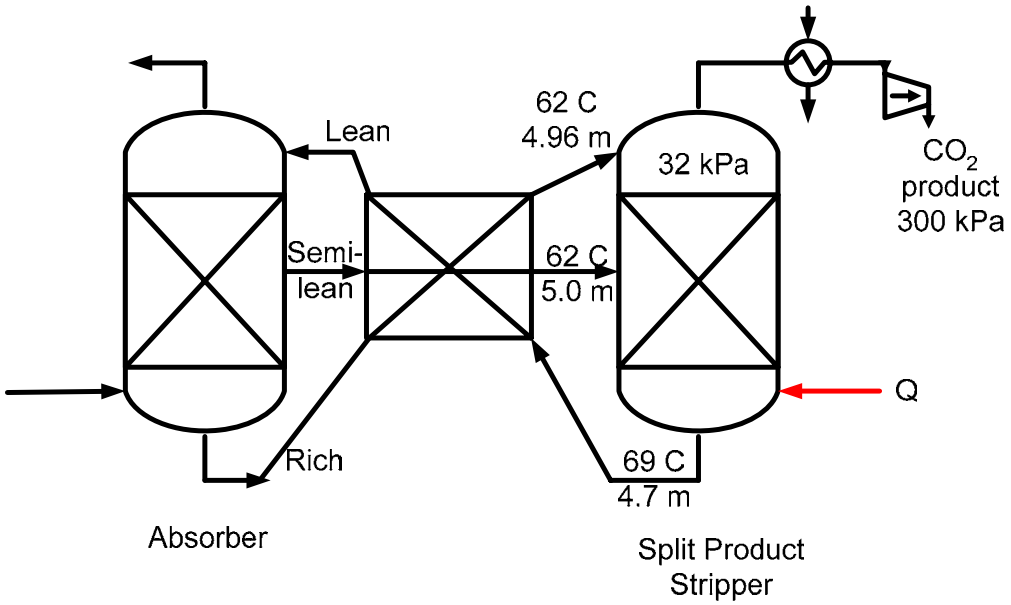

Figure 1. Vacuum Split Product.

Aspen Custom Modeler (ACM) Model

A model has been developed in Aspen Custom Modeler to simulate the stripper operation.

Modeling Assumptions

(a) The sections were assumed to be well mixed in the liquid and vapor phases.
(b) The reboiler was assumed to be in equilibrium.
(c) Negligible vaporization of the solvent.

The CO_2 vapor pressure (kPa) under stripper conditions for generic solvents is given by:

$$\ln \quad P_{CO2} = a + (b * ldg) + \frac{\Delta H}{T} \qquad (1)$$

P = the equilibrium partial pressure of CO_2 (kPa)

T = temperature (K)

ldg = mol CO_2/ mol total alkalinity (-)

ΔH = heat of desorption of the solvent (kcal/gmol CO_2)

R is the Universal gas constant (cal/K-mol)

The constant, b, is the inverse of the capacity of the solution. For the 5m K^+/2.5m PZ, the constant, a, was set to 8.82 while the constant, b, was set to 30.69. The ΔH_{des} was set to 15 kcal/gmol CO_2.

The rich CO_2 loading at specified rich P_{CO2} (kPa) leaving the absorber at 40°C for 5m K^+/2.5m PZ is shown in Table 2.

Table 2. Predicted CO_2 Solubility at Absorber Conditions.

		CO_2 loading $\left[\frac{\text{mol } CO_2}{\text{mol } K^+ + \text{mol PZ}}\right]$
Solvent	**Rich P_{CO2}* (kPa)**	**40°C**
5m K^+/2.5m PZ	1.25	0.505
	2.5	0.528
	5	0.551
	10	0.573

The heat of vaporization of water, partial pressure of water, heat capacities of steam, CO_2 and the solvent (essentially water) were calculated from equation derived from the DIPPR database.

The partial pressure of CO_2 and water on each section were calculated from equation 1

$$E_{mv} = \frac{P_n - P_{n-1}}{P_n^* - P_{n-1}} \quad (2)$$

where E_{mv} is the Murphree plate efficiency defined in terms of partial pressures

P_n, P_{n-1} is the partial pressures of the component on sections n and n-1

P_n* is the equilibrium partial pressure of the component leaving section n.

An efficiency of 40% and 100% were assigned to CO_2 and water. The model assumed 100% efficiency with respect to heat transfer.

For a given rich and lean CO_2 loading, column pressure and temperature approach in the cross exchanger, the model solves the VLE equations, material and energy balances and outputs the reboiler duty normalized by the moles of CO_2 removed, the equivalent work and the temperature, pressure and concentration profiles in the column. In order to find the minimum equivalent work, W_{eq}, required for stripping, for a fixed set of rich CO_2 loading, column pressure and temperature approach, and a range of lean CO_2 loading, the model performs sensitivity analysis by interfacing with a Microsoft Visual Basic Code. The tabulated results produced by this code allows for the lean CO_2 loading that minimizes W_{eq} to be identified.

The equivalent work is a convenient way to quantify the energy requirement of the process. It constitutes the work lost from the turbine upstream of the power plant since the condensing steam used to run the reboiler is no longer available to generate electric power. It also aids in comparing heat and work (which are different forms of energy) on an equivalent basis.

The equivalent work for stripping is given by:

$$W \text{ (kcal/gmol } CO_2) = 0.75\ Q \left[\frac{T_{cond} - T_o}{T_{cond}}\right] + W_{comp} \quad (3)$$

where Q is the reboiler duty in kcal/gmol CO_2, T_{cond} is the temperature of the condensing steam (temperature of reboiler plus 10K) in the shell of the reboiler and T_o is the temperature of the cooling water (313K). The first term on the right hand side of equation 3 constitutes the amount of work that could be produced if the steam used in running the reboiler were expanded in a Carnot Engine with 75% efficiency. W_{comp} constitutes the adiabatic work of compression of the gas exiting the top of the stripper to 1000 kPa (an arbitrary pressure selected). For this analysis isentropic efficiency of the compressor was assumed to be 75%.

Results and Discussion

Predicted Stripper Performance

The optimization of the lean loading in the two configurations, the vacuum stripper and the vacuum split product, are shown in Table 3. For the split configuration, the loading of the split stream was assumed to be the loading mid-way of the rich and the optimized lean loading for the vacuum stripper.

The results show that the vacuum configuration is more attractive than the vacuum split product configuration. A 2^oC approach is more attractive than a 5^oC approach. A closer approach may be achievable in a vacuum stripper. The optimum split product case is the limiting case when the rich loading and split stream loading coincide. Using a vacuum stripper, 90% removal cannot be achieved with the lean loading that minimizes the total equivalent work.

In order to understand the internal column operation, McCabe-Thiele plots are used. Figure 2 shows the McCabe-Thiele plot for 5m K^+/2.5m PZ at a rich loading of 0.528 mol CO_2/ mol total alkalinity for a vacuum stripper at the optimum lean loading. The total equivalent work is 8.1 kcal/gmol CO_2. It is evident that a rich end pinch occurs at this optimum condition using the three configurations. If a vacuum split configuration is used, the McCabe-Thiele plot shown in Figure 3 with a split ratio of 9:1 between the rich and the semi-lean streams also shows a rich end pinch. Figure 4 shows the McCabe-Thiele plot for a vacuum stripper in which 90% removal is achieved. It is evident that the system tends towards a rich end pinch but a rather evenly distributed driving force is observed.

Table 3. Stripper Performance with vacuum and vacuum split product configurations.

Configuration	Rich Flow	Rich ldg	Lean ldg	Split Flow	Split ldg	T_{app}	Q_{reb}	W_{eq}	Total W_{eq}	T_{reb}	CO_2 removal
	(moles)	(mol CO_2/mol Total Alk)		(moles)		(^oC)	(kcal/gmol CO_2)			(^oC)	(%)
V	1000	0.573	0.547	0	0	2	34.5	2.1	5.8	55	55
VSP	100	0.573	0.525	900	0.55	2	36.9	2.7	6.4	60	77
V	1000	0.573	0.498	0	0	2	31.7	2.6	6.3	64	90
VSP	900	0.573	0.544	100	0.55	2	34.5	2.2	5.9	56	59
V	1000	0.573	0.526	0	0	5	39.5	2.8	6.5	60	76
VSP	100	0.573	0.5	900	0.55	5	41.8	3.4	7.1	64	89
V	1000	0.573	0.498	0	0	5	35.8	3.0	6.7	64	90
VSP	900	0.573	0.522	100	0.55	5	39.3	2.9	6.6	61	79
V	1000	0.528	0.497	0	0	2	46.9	3.9	7.6	64	61
VSP	100	0.528	0.481	900	0.498	2	64.1	5.5	9.2	66	76
V	1000	0.528	0.453	0	0	2	48.2	4.4	8.1	68	90
VSP	900	0.528	0.493	100	0.498	2	47.2	4.0	7.7	65	66
V	1000	0.528	0.468	0	0	5	49.4	4.4	8.1	67	84
VSP	100	0.528	0.467	900	0.498	5	72.7	6.4	10.1	67	85
V	1000	0.528	0.453	0	0	5	49.9	4.5	8.2	68	90
VSP	900	0.528	0.468	100	0.498	5	50.2	4.5	8.2	67	84

V – vacuum; VSP - vacuum split product

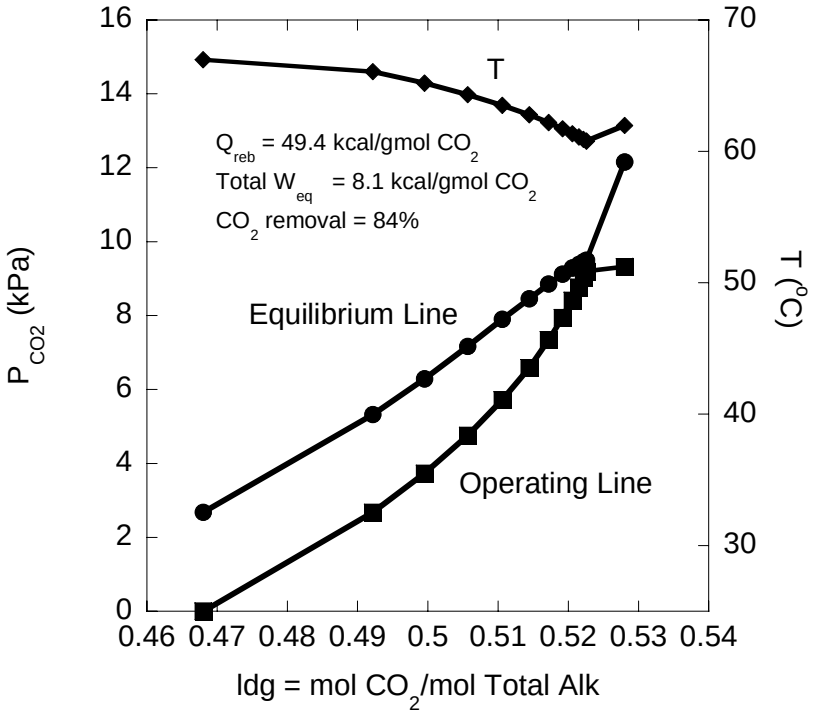

Figure 2. McCabe-Thiele Plot for 5m K^+/2.5m PZ, Vacuum Stripper (Rich P_{CO2}* = 2.5 kPa @ 40°C), T_{app} = 5°C.

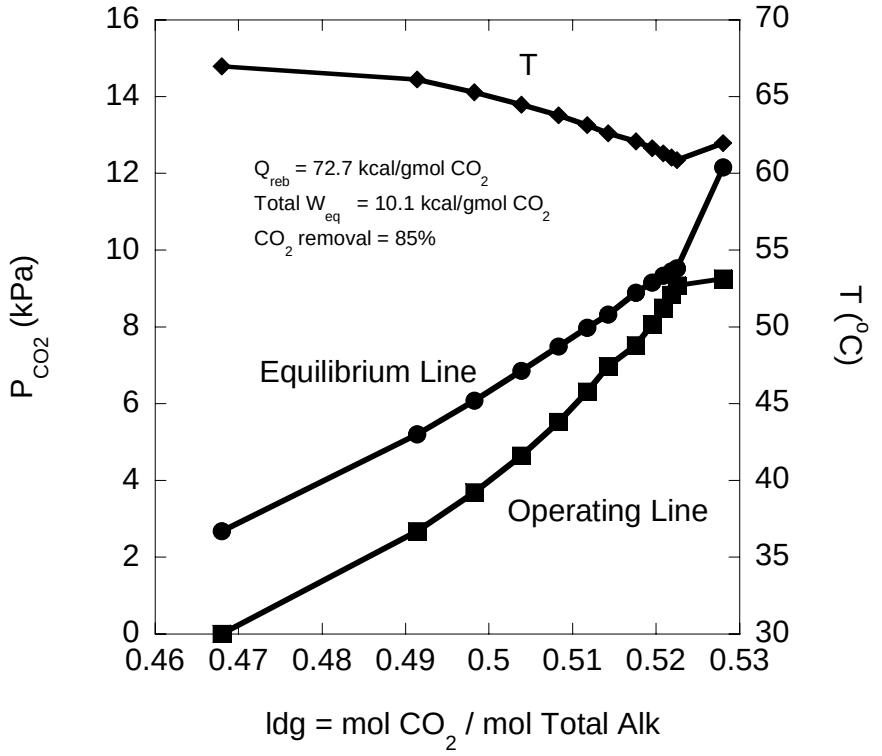

Figure 3. McCabe-Thiele Plot for 5m K^+/2.5m PZ, Vacuum Split Product Stripper (Rich P_{CO2}* = 2.5 kPa @ 40°C), T_{app} = 5°C.

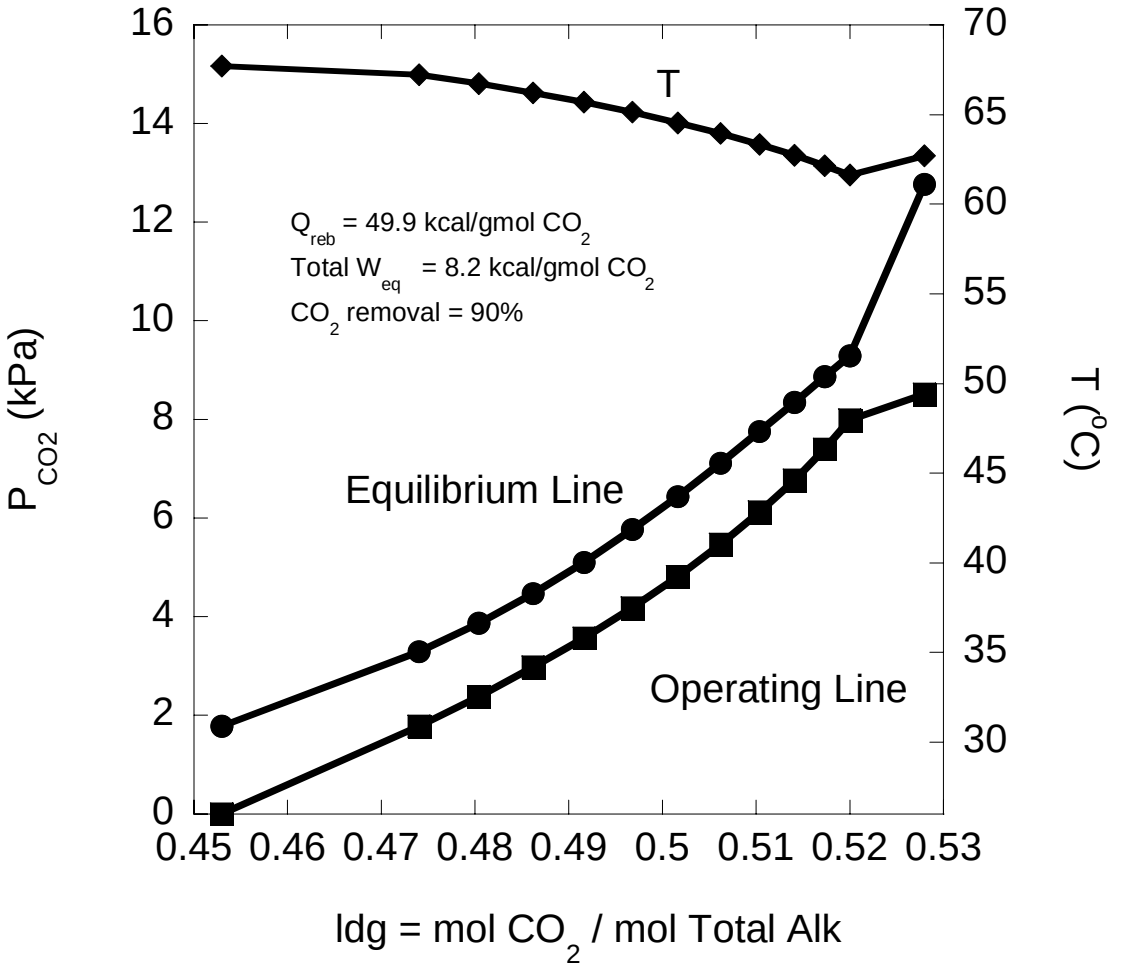

Figure 4. McCabe-Thiele Plot for 5m K^+/2.5m PZ, Vacuum Stripper (Rich P_{CO2}* = 2.5 kPa @ 40°C, 90% removal), T_{app} = 5°C.

Conclusions and Future Work

In this quarter, the ACM model was modified and extended to model simple, vacuum, multipressure and split product configurations. The vacuum stripper was compared to the split product configuration and the vacuum stripper was found to be more attractive. The optimized conditions were found to give a rich end pinch. At the optimized lean loading (i.e. lean loading that minimizes equivalent work) it was found that 90% removal was not achievable. Higher removal efficiencies could be achieved with a higher temperature approach even though a lower temperature approach reduces total equivalent work.

We are currently working on developing a mass transfer model. The results from our previous pilot plant campaigns are also been revisited to further understand the operation of the stripping column and help in fine-tuning our stripper model.

Subtask 1.10a – Simulate MEA Baseline

by Ross Dugas

(Supported by this contract)

Summary

Data obtained from the MEA baseline campaign were further analyzed to characterize absorber temperature profiles and stripper mass transfer. This report also includes experimental data for a 7m monoethanolamine/2m piperazine solvent. The experimental work was performed by Alicia Nobis, Gregory Toepperwein and Robert Trimble as an undergraduate special project. They examined ionic conductivity, pH, and density trends with respect to various temperatures and CO_2 loadings. This report is broken into two distinct parts addressing each of these subjects.

Introduction

The MEA baseline campaign was completed in April 2005. Previously reported data include material and energy balances, pressure drop and mass transfer data for the absorber, and some preliminary Aspen modeling to match pilot plant performance. This report addresses absorber temperature profiles and stripper mass transfer.

Results and Discussion

Absorber Temperature Profile

The absorber contains 7 RTD temperature sensors. The locations of the sensors are defined by the height from the bottom of the lower bed of packing. In between the two 10-foot beds of packing, there is a liquid redistribution and packing change-out area which occupies five and a half feet of the column. The location of the temperature sensors can be seen in Figure 5.

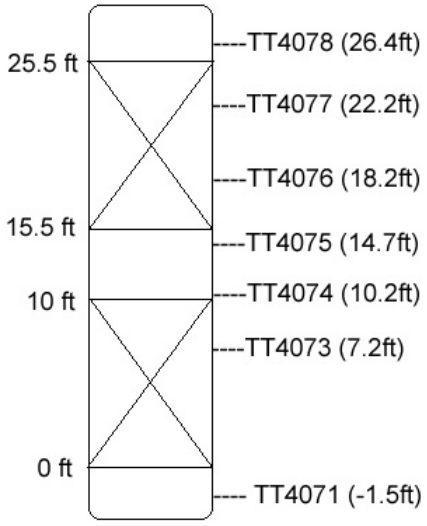

Figure 5. Absorber Temperature Measurement Locations.

The heat of reaction of CO_2 with MEA produces a temperature bulge in the column. This temperature bulge can drastically affect the absorption rates in the column since the equilibrium of the absorption reaction will shift with temperature. In severe cases where pinching occurs due to the increased temperatures, the ability of MEA ability to capture CO_2 is drastically reduced.

The temperature bulge was defined as the difference in the observed temperature and the linear temperature. This linear temperature is the expected temperature at a point in the column assuming a constant temperature gradient between temperature sensors TT4078 and TT4071. This temperature bulge definition is illustrated in Figure 6.

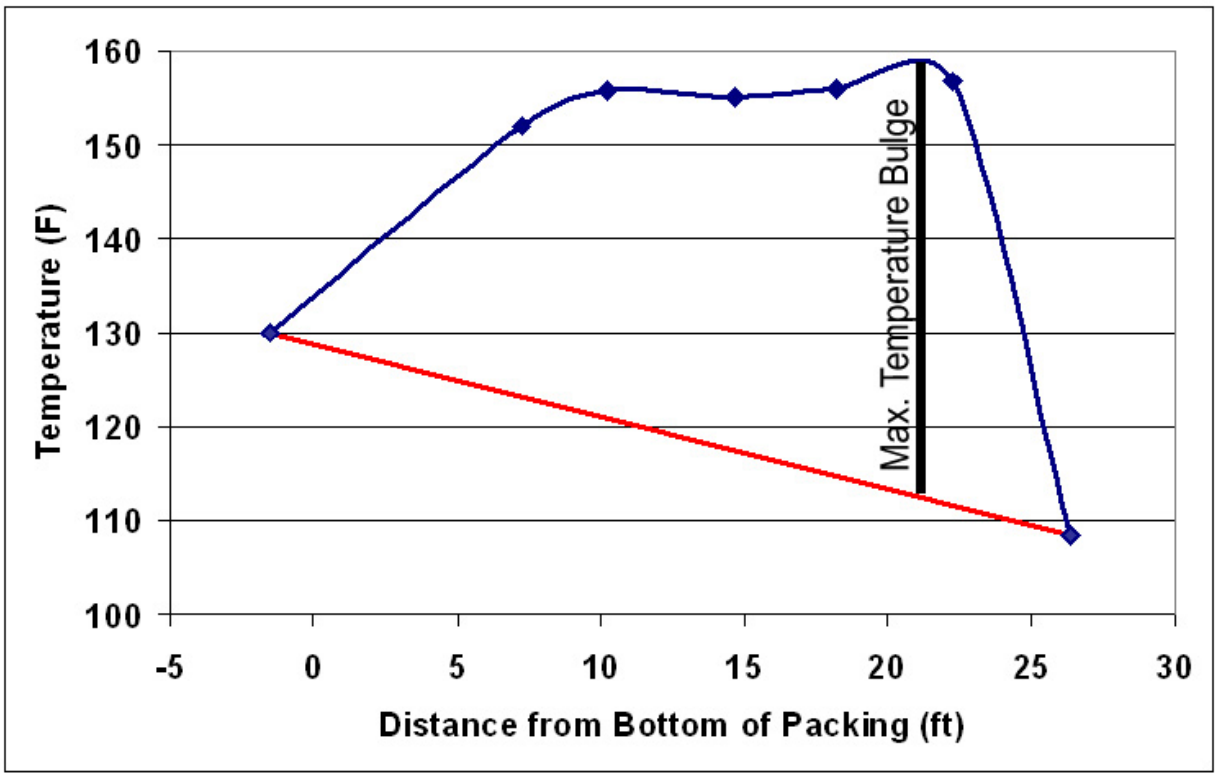

Figure 6. Absorber Temperature Bulge Diagram.

The temperature profiles could not accurately be defined by a curve fitted equation. The lack of an accurate equation to predict temperatures between sensors forces the maximum temperature bulges to be declared at one of the five interior sensors where temperatures are known. The measured temperatures, maximum temperature bulge and bulge location for each of the 48 runs can be seen in Table 4. Samples 1-24 utilized Flexipac 1Y in the absorber while runs 25-48 used IMTP #40.

Table 4. Absorber Temperatures Bulge Parameters.

Sample	Bed Temp TT4078 (F)	Bed Temp TT4077 (F)	Bed Temp TT4076 (F)	Bed Temp TT4075 (F)	Bed Temp TT4074 (F)	Bed Temp TT4073 (F)	Bed Temp TT4071 (F)	Bulge Location	Max Temp Bulge (F)	L/G (lb/lb)
1	75.5	171.7	173.2	176.9	168.4	175.6	126.4	TT4077	88.6	2.3
2	74.2	115.2	170.8	174.9	166.8	174.0	127.0	TT4076	81.1	2.2
3	70.7	167.0	168.0	173.3	165.2	172.4	117.1	TT4077	89.5	1.6
4	71.1	163.1	165.6	171.4	163.0	170.9	117.0	TT4077	85.2	1.6
5	138.0	158.9	142.4	141.3	131.6	132.1	134.0	TT4077	21.5	2.1
6	137.7	161.7	145.9	144.4	134.6	134.5	135.0	TT4077	24.4	2.1
7	126.6	172.6	165.8	163.2	152.3	146.2	110.1	TT4077	48.4	2.3
8	125.0	173.0	167.6	165.6	155.0	149.2	111.9	TT4077	49.9	2.4
9	138.1	165.1	149.2	143.6	132.5	126.9	102.5	TT4077	32.2	1.9
10	139.3	164.8	148.9	143.2	132.5	126.5	102.7	TT4077	30.9	1.9
11	140.2	157.6	139.4	134.2	125.4	119.6	98.2	TT4077	23.7	1.7
12	139.0	155.8	136.0	130.8	121.3	116.7	96.5	TT4077	23.1	1.6
13	108.8	166.0	157.4	156.6	150.6	146.4	114.7	TT4077	56.3	4.1
14	107.2	164.7	156.5	156.1	150.3	145.9	114.1	TT4077	56.5	4.1
15	94.0	109.7	120.5	128.9	127.7	140.7	125.3	TT4073	25.2	6.5
16	95.6	105.2	110.6	125.4	127.0	137.3	128.9	TT4073	18.8	7.2
17	96.6	104.7	107.7	118.7	119.6	127.4	124.8	TT4073	11.5	7.3
18	101.8	173.7	170.7	170.9	166.4	162.7	114.7	TT4077	70.0	4.4
19	94.8	172.7	170.8	171.9	167.5	165.1	116.0	TT4077	74.8	4.4
20	108.7	170.1	158.0	152.1	146.9	142.4	106.0	TT4077	61.8	3.5
21	107.3	169.1	155.6	149.3	143.8	139.7	105.1	TT4077	62.1	3.5
22	117.3	162.2	143.9	137.0	130.2	127.6	99.1	TT4077	47.6	3.1
23	118.1	161.8	142.9	135.5	128.5	125.7	98.6	TT4077	46.6	3.1
24	110.7	170.5	166.2	163.8	161.5	155.0	110.7	TT4077	59.8	3.7
25	100.8	106.9	110.7	111.4	113.6	120.5	124.5	TT4073	3.5	8.5
26	100.7	106.0	109.3	110.1	112.4	118.6	122.7	TT4073	2.8	8.5
27	96.9	111.3	118.0	118.3	121.8	132.5	127.1	TT4073	14.9	6.7
28	96.3	110.8	117.1	117.2	120.1	130.2	125.8	TT4073	13.6	6.6
29	105.3	154.5	154.3	153.8	154.8	151.8	119.5	TT4077	47.1	4.4
30	108.4	156.8	156.0	155.2	155.8	152.0	119.6	TT4077	46.7	4.4
31	89.7	110.9	118.1	115.8	123.0	141.3	126.9	TT4073	26.0	6.6
32	91.8	114.0	122.5	120.2	127.4	144.5	126.3	TT4073	29.0	6.6
33	98.9	125.6	132.7	129.6	135.4	143.8	122.9	TT4073	28.5	7.1
34	99.1	125.6	132.4	129.8	135.4	144.0	122.6	TT4073	28.7	7.0
35	90.3	106.7	112.8	110.8	115.2	131.3	126.2	TT4073	16.3	7.1
36	91.1	109.6	117.5	114.9	119.7	135.8	126.9	TT4073	20.0	6.9
37	97.1	110.1	117.2	114.9	117.6	126.5	125.2	TT4076	11.9	8.1
38	96.0	109.0	114.9	112.9	115.6	124.6	124.2	TT4076	10.7	9.2
39	95.8	108.2	113.4	114.7	118.0	129.1	130.5	TT4073	9.4	6.8
40	96.6	108.8	114.3	115.5	118.9	130.4	130.8	TT4073	10.3	6.8
41	115.4	166.6	165.7	164.8	164.8	160.5	124.8	TT4077	49.8	4.6
42	118.1	167.3	166.4	165.6	165.5	161.1	125.0	TT4077	48.2	4.6
43	135.0	160.3	156.0	153.4	151.2	143.2	112.0	TT4074	29.6	3.2
44	136.7	161.1	156.8	153.8	151.7	143.6	112.5	TT4074	29.0	3.2
45	96.6	110.4	117.2	118.7	123.6	142.3	135.0	TT4073	19.4	6.7
46	97.3	109.4	115.2	116.2	119.8	135.4	134.5	TT4073	12.6	6.7
47	136.7	160.2	154.9	152.2	148.6	142.8	112.4	TT4077	27.1	3.4
48	134.8	158.7	153.7	151.2	147.6	141.8	111.4	TT4077	27.3	3.4

The maximum temperature bulge ranged from 3 to 90°F depending on the operating conditions. In most of the conditions with the Flexipac 1Y packing, the temperature bulge was observed at the top of the column. However, the temperature bulge was typically at the bottom of the column for the IMPT #40 packing. The difference in the bulge location is linked to the L/G ratios that were used for each packing. Since Flexipac 1Y has approximately 3 times more area than IMTP #40, lower L/G ratios were used for similar CO_2 removal performances. This L/G ratio effectively causes the majority of the reaction to occur at the top of the column. The relationship between the temperature bulge location and the L/G ratio can be seen in Figure 7.

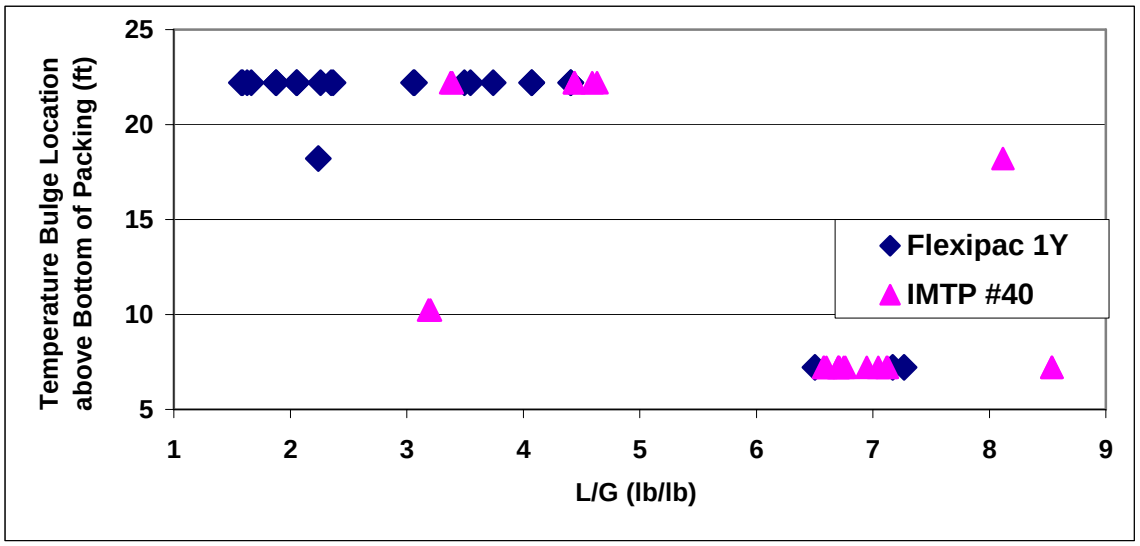

Figure 7. Maximum Temperature Bulge Location Dependence on L/G Ratio.

Figure 7 shows that runs with L/G ratios lower than 5 typically showed a maximum temperature bulge at the top of the absorber while L/G ratios greater than 6 usually gave maximal temperature bulges near the bottom of the column. Runs with lower L/G ratios generally had a richer rich loading. Runs with the Flexipac 1Y packing were typically too rich near the bottom of the absorber to provide significant driving forces for additional reaction. The IMTP #40 runs suggest that the rich solutions provide the largest driving force near the bottom of the absorber where gaseous CO_2 concentrations are highest. The relationship between rich loading and temperature bulge location can be seen in Figure 8.

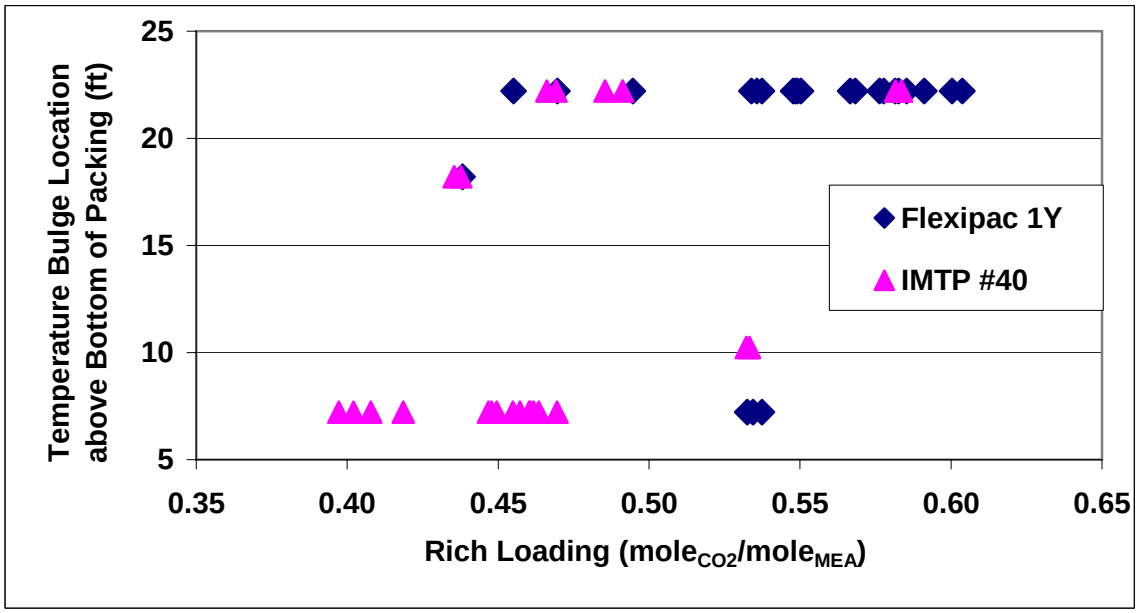

Figure 8. Maximum Temperature Bulge Location Dependence on Rich Loading.

Figure 8 shows that runs containing IMTP #40 in the absorber generally achieved lower rich loadings than Flexipac 1Y. It also shows that runs resulting in rich loadings lower than 0.47 typically showed temperature bulges near the bottom of the column while rich loadings greater than 0.47 generally resulted in temperature bulges near the top of the column.

Stripper Mass Transfer

Mass transfer data for the stripper were obtained from the CO_2 driving forces at the top and bottom of the stripper. The CO_2 concentration at the top of the stripper was obtained by using the water vapor concentration. The gas at the top of the column was assumed to be saturated. The water vapor pressure was calculated from the temperature at the top of the column. The remaining pressure was assumed to be CO_2. At the bottom of the column, the operating CO_2 concentration was taken as 0 since the CO_2 vapor content is very close to 0 at the bottom of the column. The equilibrium CO_2 vapor pressure at the top and bottom of the column was determined using a flash calculation in Aspen using the electrolyte NRTL properties with Freguia's Fortran code. The flash routine took into account the temperature and composition of the stream. Using the driving force at the top and bottom of the stripper, a log mean driving force was calculated. Mass transfer coefficients were calculated by Equation 4.

$$K_G a = \frac{CO_2 Desorbed}{\Delta P_{lm} \cdot Volume_{Packing}} \tag{4}$$

In Equation 4, $K_G a$ is defined in mol/(m^3·s·kPa). CO_2 desorbed is obtained from the mass balance and has units of mol/s. The log mean driving force and the volume of the packing are in kPa and m^3, respectively. Calculated mass transfer coefficients were best correlated with the rich loading entering to top of the stripper. This correlation can be seen in Figure 9.

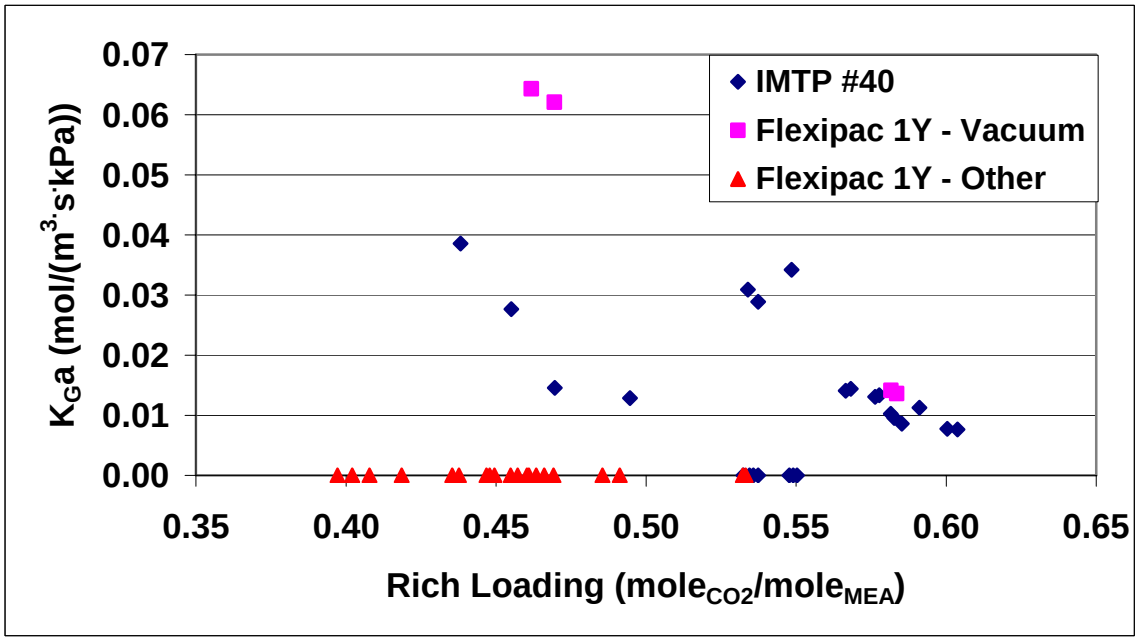

Figure 9. Stripper Mass Transfer Dependence on Rich Loading.

Figure 9 shows two distinct trends between K_Ga and the rich loading. The trend with lower loadings consisting of only four points is possibly in error. Those four runs were the first four runs of the campaign. Those conditions were very similar to other runs later in the campaign which followed the other trend. It is possible that some data collection was inaccurate at the very beginning of the campaign. Figure 9 also shows that approximately half the points report a mass transfer coefficient of zero. This is due to the calculation of the log mean driving force. For many runs, especially those with Flexipac 1Y in the stripper, the Aspen flash calculation reported lower equilibrium CO_2 vapor pressures than operating CO_2 pressures. This gives a negative CO_2 driving force so the log mean driving force and the mass transfer coefficients could not be calculated. This negative CO_2 driving force at the top of the stripper suggests that either the Aspen flash calculation is incorrect or the stripper is absorbing CO_2 at the top of the column. Since the stripper feed was consistently subcooled due to inadequate preheating, it is not unreasonable that the stripper could absorb some CO_2. It is logical that most of these runs with absorption at the top of the stripper occurred for the Flexipac 1Y packing. When Flexipac 1Y was in the stripper, IMTP #40 was in the absorber. IMTP #40 has approximately 3 times less surface area and generally achieves lower rich CO_2 loadings than Flexipac 1Y. This lower rich loading combined with a subcooled feed could possibly result in absorption in the stripper. The only Flexipac 1Y runs that did not report absorption in the stripper were the four runs with vacuum stripping. Those runs encountered much lower gaseous CO_2 concentrations since the total pressure of the stripper was lowered from 23.5 to 10 psia.

Conclusions

The maximum temperature bulge in the absorber ranged from 3 to 90°F in the 48 runs of the MEA baseline campaign. In the majority of runs with Flexipac 1Y in the absorber, the maximum temperature bulge was observed at the top of the absorber. Runs with IMTP #40 generally showed the maximum temperature bulge at the bottom of the absorber. This difference is due to the increased performance of Flexipac 1Y packing. Runs with the Flexipac 1Y packing had smaller L/G ratios and produced richer rich solutions. Runs with L/G ratios less than 5 usually produced maximum temperature bulges at the top while ratios greater than 6 usually produced maximum temperature bulges at the bottom of the absorber.

Mass transfer coefficients for the stripper decreased linearly with increasing rich loading. The first four runs of the campaign seem to show inconsistent mass transfer performance with respect to the majority of the runs. For many cases, especially runs with Flexipac 1Y, mass transfer coefficients could not be calculated. Calculations showed that these runs were absorbing CO_2 in the top of the stripper. This is possible since many of these runs have low lean loadings and enter the stripper at relatively low temperatures.

Subtask 1.10b – Property Data for MEA

by Ross Dugas

(Supported by this contract)

Introduction

Experimental data for a 7m monoethanolamine/2m piperazine solvent was obtained by Alicia Nobis, Gregory Toepperwein and Robert Trimble. They examined ionic conductivity, pH, and density trends with respect to various temperatures and loadings.

Experimental

A 7 molal monoethanolamine/2 molal piperazine solution was prepared. This solution was then split roughly in half. Half was covered with parafilm and labeled as solution #1. The other half was sparged with CO_2 for 2 hours and labeled solution #5. Solutions 2, 3 and 4 were created according to Table 5.

Table 5. Make-up of Small Volume Test Solutions.

Solution	Origin
1	Unloaded Standard (#1)
2	12g Solution #1, 4g Solution #5
3	8g Solution #1, 8g Solution #5
4	4g Solution #1, 12g Solution #5
5	Loaded Standard (#5)

Ionic conductivity, pH, density and carbon content were measured across the desired temperature range. Carbon content is sometimes converted to a CO_2 loading. Loadings of this solution are defined as the moles of CO_2 divided by the moles of amine equivalents. Since piperazine has 2 equivalents per mole, the loading can be represented in mole terms as CO_2/(MEA+2Pz). The samples were heated on a hot plate and the temperature was monitored by a thermocouple built into the conductivity meter. To prevent the loss of CO_2, MEA, or piperazine (PZ) during heating, the test fluids were covered with parafilm. The parafilm was loosely attached to allow excess pressure to bleed off while still minimizing material loss. Once a solution was at the desired temperature, the pH and ionic conductivity were recorded. A 50 µL aliquot was dissolved into 5 mL of deionized water and mixed thoroughly. From this dilution, five 50 µL injections were made into the TOC and recorded.

Large volume test solutions were also created for density measurements with a hydrometer. Conductivity, carbon content and pH were also tested on this large volume test solution. The same large volume solution was tested for density at each loading. The amount of CO_2 added was determined by leaving the solution on a scale while the CO_2 was sparging it. The added mass was assumed to be the mass of CO_2 absorbed into the solution.

Results

The large volume results seemed to show more trustworthy data in general. This is probably because the small volume samples can lose a higher percentage of CO_2 faster due to their smaller inventories. In particular, the CO_2 concentrations for the small samples were not as reproducible as the large sample measurements. Since the large sample measurements seem to be superior, only those results are presented in this report. The large volume solution data can be seen in Table 6.

Table 6. Large Volume Property Measurements for the 7m MEA/2m PZ Solvent.

Sparge #	Temp (°C)	Peak Area	Carbon Injected (µmol)	CO_2 Molarity (M)	Loading ($mol_{CO2}/mol_{amine\ equiv}$)	Conductivity (mS/cm)	pH	Density (kg/m^3)
0	25	-	-	-	-	0.29	11.73	1020
0	35	-	-	-	-	0.42	11.42	1015
0	45	-	-	-	-	0.60	11.13	1010
0	55	-	-	-	-	0.78	10.88	1006
0	60	-	-	-	-	0.88	10.66	1002
1	25	2.57	0.44	0.88	0.13	8.25	10.69	-
1	35	2.33	0.39	0.78	0.11	11.0	10.36	1050
1	45	2.24	0.37	0.74	0.11	14.2	10.10	1047
1	55	2.50	0.43	0.85	0.12	17.7	10.01	1042
1	60	2.43	0.41	0.82	0.12	19.4	9.75	1039
2	25	5.32	1.01	2.01	0.29	13.8	10.25	-
2	35	5.77	1.10	2.20	0.32	18.5	10.08	-
2	45	5.47	1.04	2.08	0.30	23.6	9.86	-
2	55	5.27	1.00	1.99	0.29	29.2	9.40	-
2	60	5.35	1.01	2.03	0.29	32.0	9.17	-
3	25	7.90	1.54	3.08	0.44	14.4	9.77	-
3	35	8.83	1.73	3.46	0.50	22.6	9.38	-
3	45	8.44	1.65	3.30	0.48	28.9	9.12	-
3	55	8.29	1.62	3.24	0.47	35.9	8.90	-
3	60	8.00	1.56	3.12	0.45	39.9	8.85	-
4	25	9.81	1.93	3.86	0.56	17.4	8.80	-
4	35	9.90	1.95	3.90	0.56	23.8	8.56	-
4	45	9.76	1.92	3.84	0.55	31.2	8.36	-
4	55	9.84	1.94	3.88	0.56	39.1	8.17	-
4	60	17.44	3.50	-	-	43.3	8.06	-

CO_2 Loading

The largest concern of these measurements was the loss of CO_2. When dealing with the large volume solutions, the solution showed wide variations in the CO_2 concentration for the last sparging. The 5^{th} sparging is left out of the data in this report. The results of the loadings from the other 4 spargings can be seen in Figure 10.

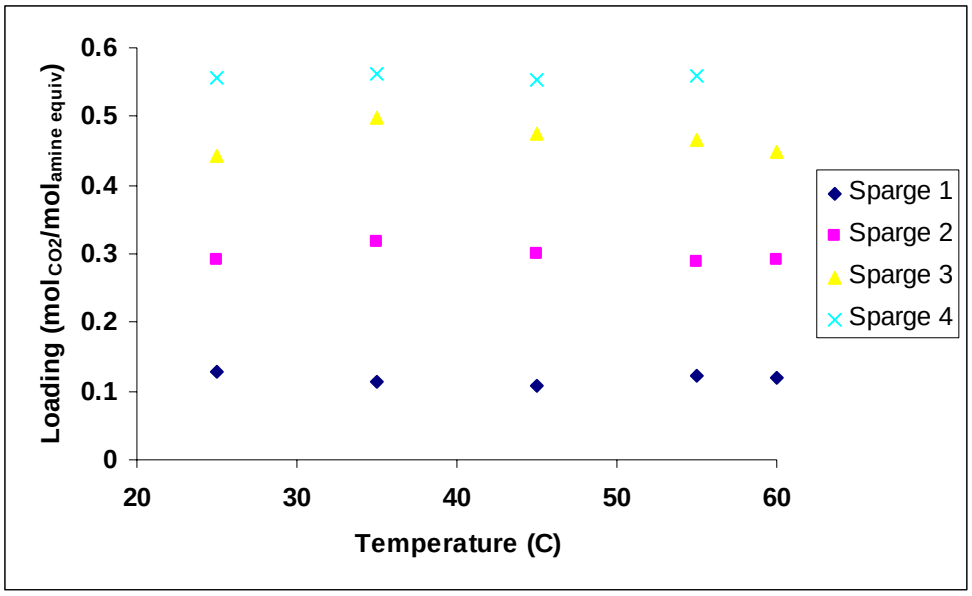

Figure 10. CO_2 Loss for 4 CO_2 Loadings with a 7m MEA/2m PZ Solvent.

Since loadings are relatively constant across temperatures for each sparging, the data scattering is more likely associated with the TOC dilutions and measurement than changes in solution composition.

Ionic Conductivity

Ionic conductivity showed a slight exponential dependence with temperature. It also showed a slight exponential dependence with loading. These dependences can be seen in Figures 11 and 12.

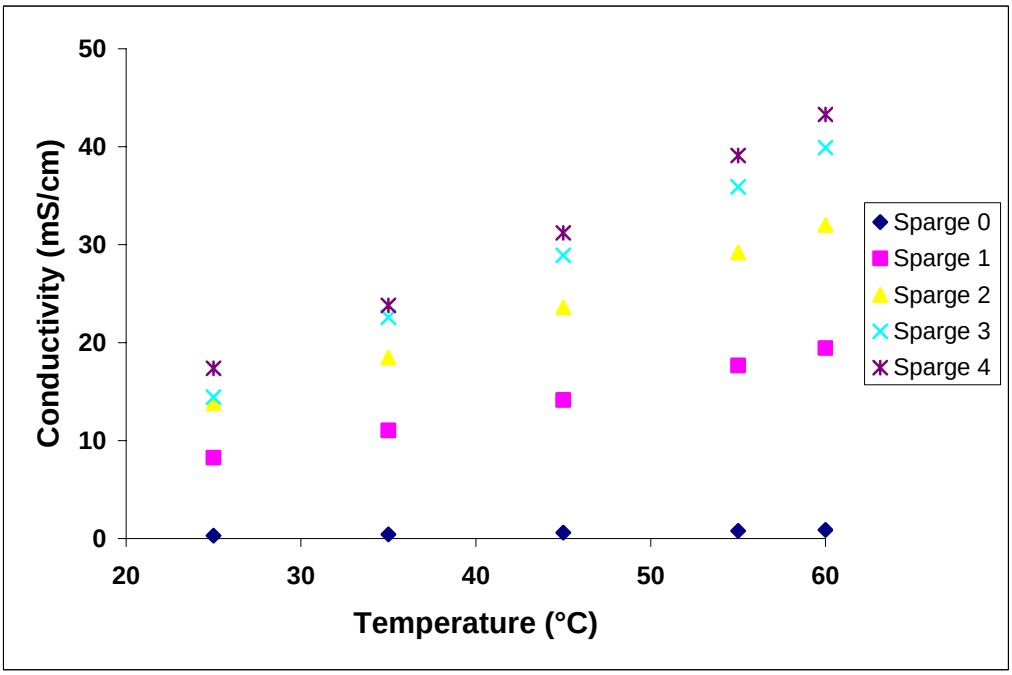

Figure 11. Conductivity Dependencies on Temperature with a 7m MEA/2m PZ Solvent.

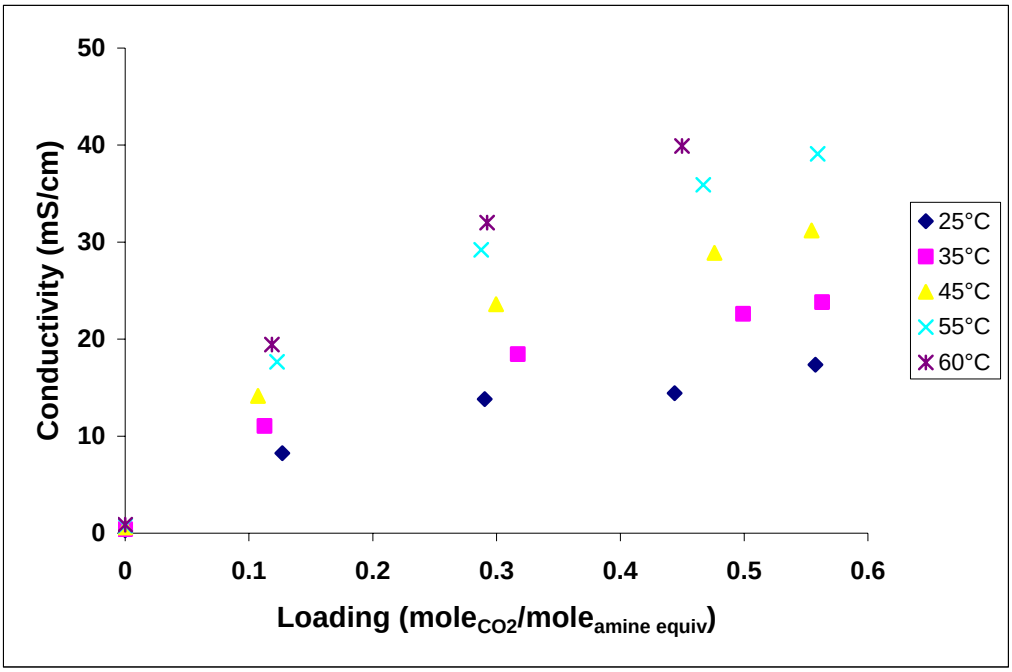

Figure 12. Conductivity Dependencies on Loading with a 7m MEA/2m PZ Solvent.

pH

The pH of the test samples was recorded at the same conditions as the ionic conductivity. The pH shows a linear dependence on temperature but a more complex dependence on loading. The solutions acidity seems to rapidly increase between 0 and 0.1 loading and also 0.4 and 0.5 loading. pH dependencies on temperature and loading can be seen in Figures 13 and 14, respectively.

Density

Density measurements were also obtained from the large volume samples. Densities could only be measured for loadings of 0 and 0.125 due to the range of the hydrometers used. Density seems to be much more dependent on loading than temperature. Recalling Figure 10, sparge 1 has a loading of approximately 0.125 while sparge 0 is unloaded. Measured densities for the two loadings can be seen in Figure 15.

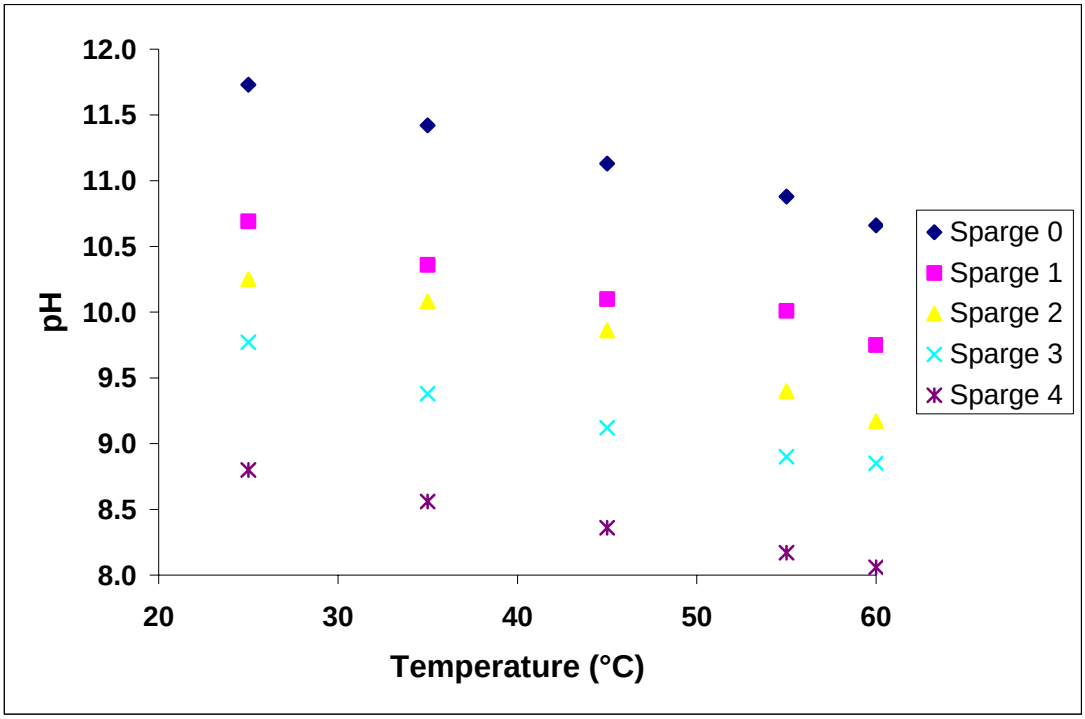

Figure 13. pH Dependencies on Temperature with a 7m MEA/2m PZ Solvent.

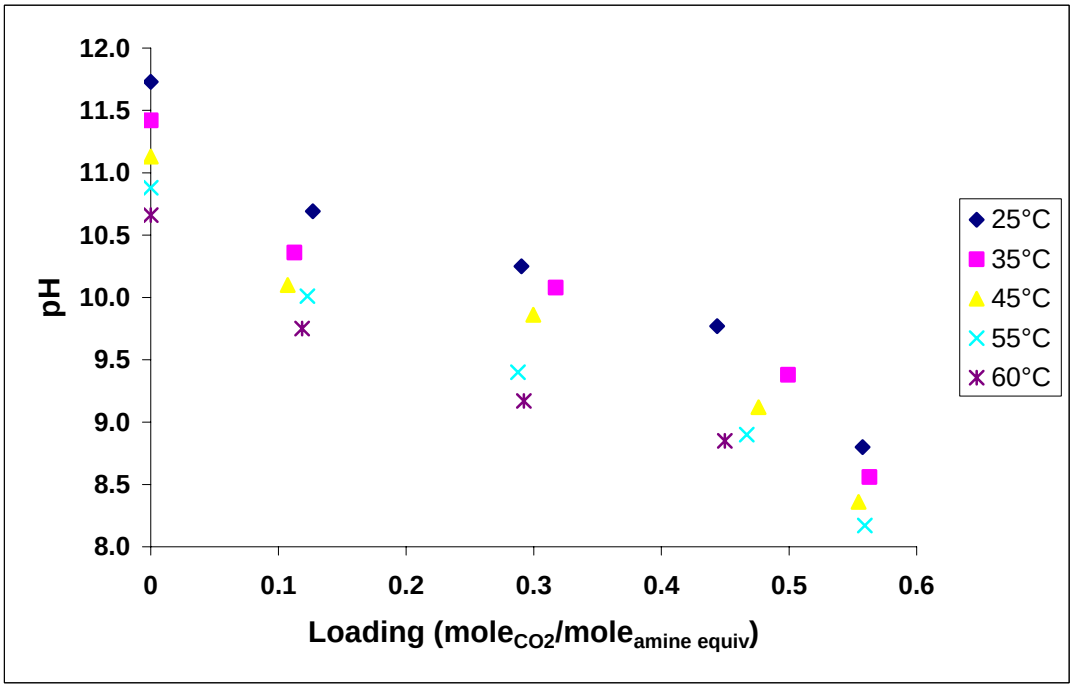

Figure 14. pH Dependence on Loading with a 7m MEA/2m PZ Solvent.

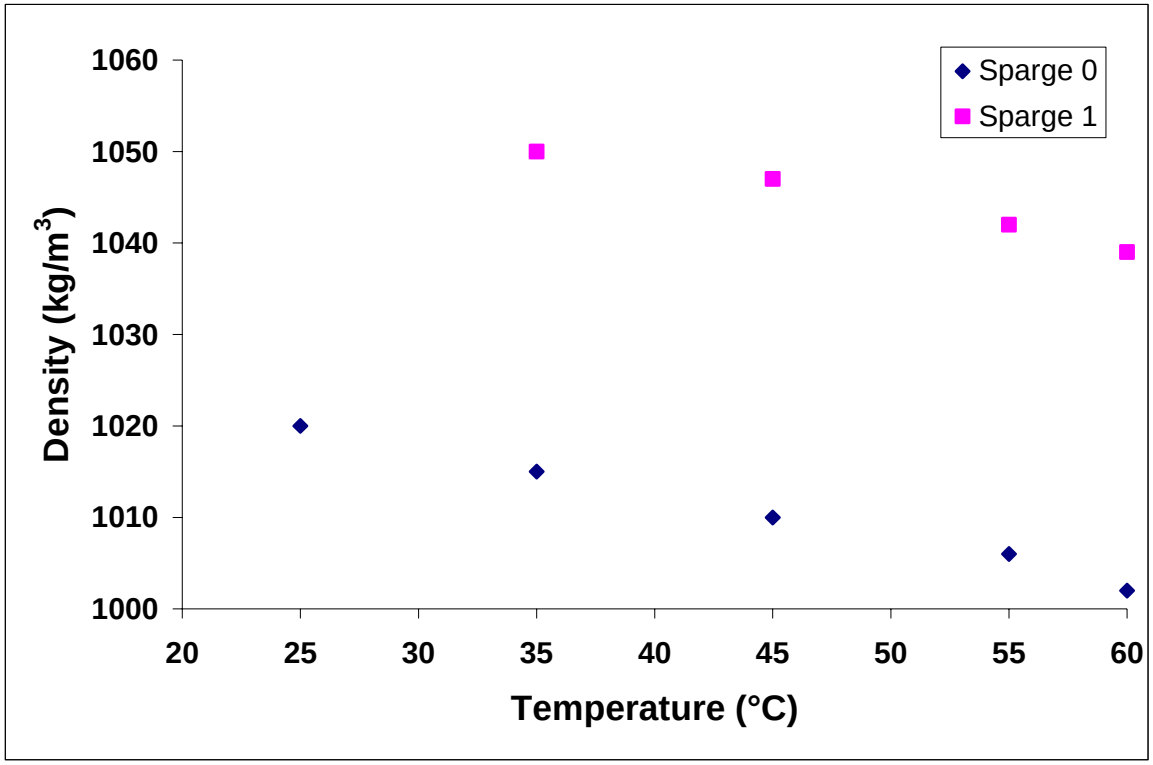

Figure 15. Density Trends for Temperature and Loading with a 7m MEA/2m PZ Solvent

Conclusions

The experimental results showed significant progress towards developing an online method to predict loading. The experimental results were found to match theoretical expectations. The ionic conductivity of the solution showed a Boltzmann dependence on temperature and saturation behavior with loading. The pH of the solution varied linearly with temperature and had a buffer-response to loading. Lastly, the density seemed to vary linearly with temperature. While a linear density dependence was expected for loading, insufficient sample data was available to verify this trend.

Task 2 – Pilot Plant Testing

Subtask 2.6 – Campaign 4

by Eric Chen

(Supported by EPA STAR Fellowship)

Introduction

In this reporting period, modifications to the pilot plant were completed and a test plan was submitted to DOE for approval. In addition, an apparatus was constructed to make density measurements between 40 to 60 ^{o}C. A new method was also developed on the Ion Chromatography analyzer to measure piperazine and potassium. Finally, bench-scale measurements of pH were taken for the 6.4 m K^{+} / 1.6 m Piperazine solvent over 4 different loadings and temperatures ranging from 40 to 60 ^{o}C.

Experimental - Pilot Plant Modifications

The final modifications to the pilot plant were completed at the end of December. The plate and frame cross exchanger was installed upstream of the existing pre-heater. The cross exchanger will use the lean stream exiting the reboiler to pre-heat the rich stream entering the stripper. The old pre-heater was converted for use as a trim heater. And the existing solvent cooler will function as a trim cooler. Existing pipes lines were rerouted to accommodate the new exchanger.

All of the existing PVC gas lines were replaced with 304L stainless steel pipe. Additional penetrations were made to accommodate various instrumentation and sample points. A new 1-inch stainless steel gas line was installed, which ran from the top of the 6-inch reboiler and into an injection port just upstream of the absorber inlet. The gas line is insulated with fiberglass.

The carbon filter was installed just downstream of main bag filter on the lean stream of the absorber. Isolation valves were installed at the inlet and outlet of the filter system to facilitate activated carbon and bag filter change-out. The first filter contains the activated carbon and a second bag filter downstream removes any carbon fines that may have escaped the carbon cylinder. A rotameter downstream of the filters, measures and controls liquid flow through the carbon filter.

Experimental - Temperature Variation of Density Measurements

Previous density measurements of the piperazine promoted potassium carbonate solvent were limited to a temperature of 40 ^{o}C. It was desired to measure the density of the solvent over a temperature ranging from 40 to 60 ^{o}C. Hydrometers from Fisher Science were procured. A cylindrical water tank was constructed out of Plexiglas. A water bath was used to heat the water and circulate the warm water through the water tank. To make a density measurement, approximately 300mL of solvent was poured into a graduated cylinder. The hydrometer was

placed in the graduated cylinder, which was then immersed in the heated water tank. A K-type thermocouple measure the temperature of the solvent and a magnetic stir bar was used to mix the solvent and maintain a uniform temperature throughout the cylinder. The stir bar was turned off when density measurements were recorded. Density measurements were taken for the 5 m K^+/ 2.5 m PZ solvent and for the 6.4 m K^+/ 1.6 m PZ solvent at two different loadings. In addition, a density measurement was taken for the pilot plant solution.

Experimental - Ion Chromatography

A new IC column was purchased and installed in the ion chromatography analyzer. The new column was better suited for piperazine and amine analysis. A new method was developed for measuring piperazine and potassium on the IC. The method takes approximately 5 minutes and uses 6 mM and 55 mM monosulphonic acid (MSA) for the eluent. The standards contained both piperazine and potassium and a calibration curve was generated over the following range of concentrations: 0 ppm K/Pz, 10 ppm K/Pz, 20 ppm K/Pz, 30 ppm K/Pz, 40 ppm K/Pz, and 50 ppm K/Pz. Concentrated pilot plant solutions from Campaign 1 were diluted by a factor of 4000. Prediluted pilot plant samples from Campaign 2 were diluted by a factor of 1000.

Experimental - pH Measurements

Bench-scale measurements of pH were made for the 6.4 m K^+/ 1.6 m PZ solvent at four different CO_2 loadings and over a temperature range from 40 to 60 ^oC. The pH measurements will be used in the pilot plant operations for controlling lean loading to the absorber. Measurements were made with a Cole Parmer pH meter.

Results

The results from the density measurements show that density decreases linearly with an increase in temperature (Figure 16). Figure 16 also shows that density is not very sensitive CO_2 loading and piperazine concentration, which corroborates the density measurements made by Cullinane on a densitometer instrument.

Tables 7 through 9 show the results from the analysis using the newly developed IC method. The results show that total alkalinity was not as well correlated to density measurements as previously assumed, which was based on Campaign 1 data. The total alkalinity results on the IC from Campaign 1 and Campaign 2 seem to show good agreement with the total alkalinity values obtained using the acid titration method used in those campaigns. Table 9 seems to show that there was some loss of potassium between the transition from Campaign 2 to the current campaign. The pilot plant samples were taken from the bottom of a large storage tank and therefore, may not have been a representative sample.

Finally, Figure 17 shows bench-scale measurements of pH dependence on CO_2 loading at different temperatures. The trends indicate that there is inconsistent variation of pH with temperature. However, pH does vary with CO_2 loading. The general slope of the bench-scale measurements can be used to determine online CO_2 loading values of the pilot plant once a pH and corresponding CO_2 loading value is established.

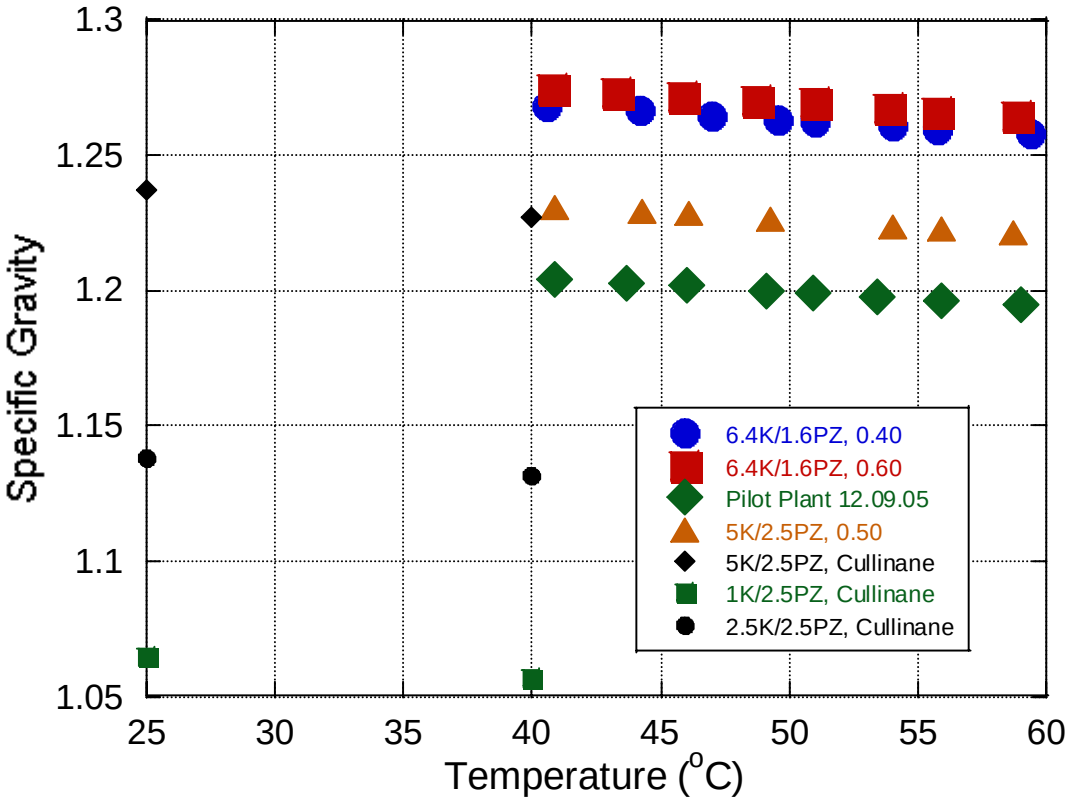

Figure 16. Density Dependence on Temperature.

Table 7. Campaign 1 IC Results.

Campaign 1 Data	K mol/kg	PZ mol/kg	Talk mol/kg	K/PZ	Density kg/m3
C1 6/16 1700	2.3293	1.5802	5.4896	1.4741	1146.6
C1 6/17 1300	2.5907	1.4356	5.4619	1.8046	1162.4
C1 6/22 1745	3.2496	1.634	6.5177	1.9887	1206.1
C1 6/22 1930	3.2348	1.6258	6.4864	1.9897	1206.4
C1 6/23 0815	3.2509	1.6377	6.5263	1.9851	1212.6
C1 6/23 1810	3.3146	1.6624	6.6393	1.9939	1211.9
C1 6/24 AL 1730	3.3365	1.5987	6.5339	2.087	1228.1

Table 8. Campaign 2 IC Results.

Campaign 2 Data	K mol/kg	PZ mol/kg	Talk mol/kg	K/PZ	Density kg/m3
C2 AL8	2.8981	1.2421	5.3823	2.3332	1224.3
C2 AL11	3.0807	1.3216	5.724	2.331	1228.2
C2 AL13	2.908	1.2493	5.4066	2.3278	1227
C2 AL14	2.7736	1.205	5.1836	2.3018	1226.2
C2 AL16	3.085	1.327	5.739	2.3248	1228.4
C2 AL22	2.9487	1.2591	5.4669	2.3418	1230.4
C2 AL37	3.2303	1.3927	6.0158	2.3194	1224.4
C2 AL38	3.027	1.3038	5.6346	2.3218	1219.5
C2 AL43	2.9179	1.2404	5.3987	2.3523	1229.1
C2 AL 26	2.8967	1.2393	5.3753	2.3373	1228.5

Table 9. Pilot Plant Results Before Start-up.

Pilot Plant 12.09.05	K mol/kg	PZ mol/kg	Talk mol/kg	K/PZ	Density kg/m3
	3.0208	1.5888	6.1983	1.9013	1204

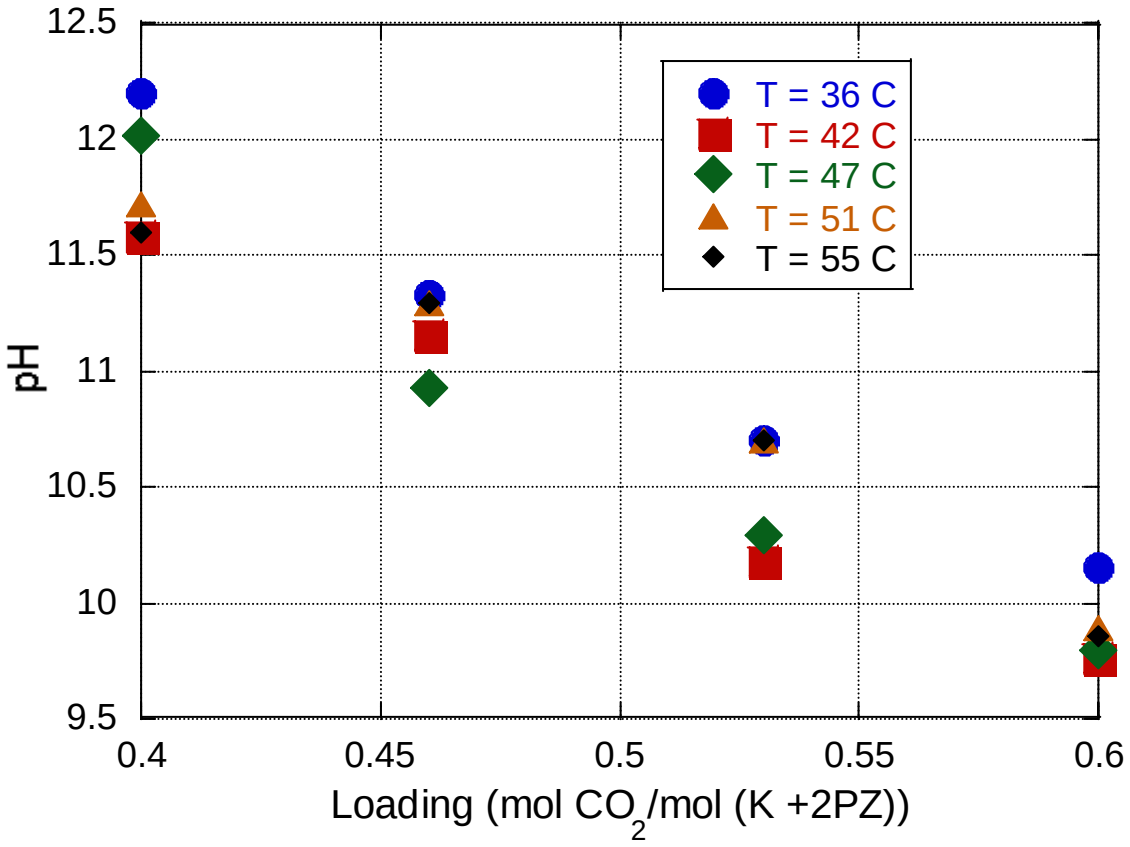

Figure 17. Bench-scale pH Measurement of 6.4mK/1.6mPZ Solvent.

Conclusions and Future Work

The final modifications to the pilot plant have been completed, and troubleshooting for Campaign 4 will commence at the beginning of January. The bench-scale measurements show that at over a temperature range of 40 to 60 ^{o}C, density decreased slightly an increase in temperature. The bench-scale measurements also show that the CO_2 loading and piperazine concentration does not strongly affect density. The results from the IC confirmed the total alkalinity values obtain by the titration method used in the first 2 campaigns. Finally, a slope for the loading dependence of pH was established and will be used for maintaining online CO_2 loading in Campaign 4.

Troubleshooting for Campaign 4 will begin in early January and the pilot plant should resume operation the second week of January. The final campaign should be completed by the end of January and the sample will be analyzed for CO_2 loading and piperazine and potassium concentration.

Task 3 – Solvent Losses

Subtask 3.1a – Analysis of Degradation Products

Andrew Sexton

(Supported by the Industrial Associates Program in CO_2 Capture)

Introduction

This effort is an extension of work by George Goff on the oxidative degradation of MEA. Goff showed that oxidative degradation can be mass-transfer limited by the physical absorption of O_2 into the amine and not by reaction kinetics. Goff also theorized that the oxidative degradation of MEA produced volatile ammonia as well as a host of other proposed degradation products. The major degradation products among these include formic acid, acetic acid, oxalic acid and glycolic acid. The oxygen stoichiometry necessary to produce these degradation products varies for each individual component; overall, it varies anywhere from 0.5 to 2.5 (Goff, 2004). Goff's work on MEA degradation was limited to analyzing MEA degradation rates via the evolution of NH_3. The ammonia evolution rates were measured using a Fourier Transform Infrared (FT-IR) analyzer.

This effort will extend Goff's gas-phase analysis by applying various methods of liquid-phase analysis, specifically ion chromatography and nuclear magnetic resonance. These analytical methods will be used to quantify the rate of amine degradation as well as the rate of degradation product formation.

The oxidative degradation of the amines may significantly affect the economics and environmental impact of these solvent systems. Oxidative degradation results in fragmentation of the amine solvent. The identity and quantity of degradation products is required to assess their impact on the environment and the process economics and to design for corrosion prevention and solvent reclaiming.

Experimental

Ion chromatography is the most extensively used liquid-phase analytical method. Anion chromatography utilizes a recently purchased AS15 (a low-capacity column designed to separate low-molecular weight anions, specifically acetate, glycolate, and formate) IonPac column made by Dionex. The column operates as a miniature adsorption tower. An unknown solution is injected into the column. An eluent of sodium hydroxide is continuously passed through the column to flush anions off the column and replenish it with hydroxide ions.

The ions leave the column and then pass through a suppressor, which provides a steady supply of H^+ ions. As a result, all other cations are flushed out of the system as waste, leaving a weakly ionized solution of H^+ ions and the unknown anion(s) in water. This solution is passed through a conductivity meter, which provides a signal peak with a specific height and area dependent upon the concentration of the anion in solution (Wang, 2005). Refer to the July 2005 quarterly report for a detailed description of the method.

The cation chromatograph, located in the CPE building, operates in a similar manner. It utilizes a CS17 IonPac column manufactured by Dionex; it is a packed column containing a divinylbenzene/ethylvinylbenzene resin that separates cations based on their affinity for the

resin. The eluent is methanesulfonic acid, or MSA (CH_3SO_3H), and the suppressor produces a steady supply of OH^- ions to flush out all other anions as waste. The end result is a weakly ionized solution of the unknown cation(s) and OH^- ions in water (Dionex, 2005). The anion IC is being used to quantify rates of degradation product formation (organic acids, nitrites, and nitrates), while the cation IC is primarily for characterizing the rate of amine degradation.

Nuclear magnetic resonance, or NMR, identifies unique ^1H atoms and/or ^{13}C atoms based on structure (double/triple bonds, attachment to acid/amine/etc. groups). Sealed liquid samples are subjected to a magnetic pulse, and each unique atom is characterized by a "chemical shift" on the readout. If the structure(s) in the solution is unknown, it may be necessary to construct a 2-D carbon-hydrogen correlation in order to determine structure. Samples must be prepared with approximately 10% D_2O (by weight) and DSS (Shoulders, 2005). D_2O, or deuterium oxide, is heavier than water and enhances the signal, thereby making the analysis easier. DSS, or Sodium 2,2-Dimethyl-2-Silapentane-5-Sulfonate, is used as a reference peak for aqueous solutions containing organic materials.

Results

During the previous quarter, degradation product formation rates were quantified from MEA and piperazine degradation. Three separate degradation experiments were analyzed for degradation product formation rates:

1. December 2004 MEA experiment (Oxidative degradation of 7 m MEA, 55°C, 1400 RPM, 0.2 mM Cu, 0.4 moles CO_2/mol MEA, 98%O_2/2%CO_2).
2. September 2005 MEA experiment (Oxidative degradation of 7 m MEA, 55°C, 1400 RPM, 0.2 mM Cu, 0.2 mM Fe, 0.4 moles CO_2/mol MEA, 98%O_2/2%CO_2).
3. November 2005 MEA experiment (Oxidative degradation of 2.5 m piperazine, 55°C, 1400 RPM, 350 ppm V^+, 98%O_2/2%CO_2).

The amine solutions were oxidized for 12 to 14 days in a low-gas flow jacketed reactor at 55°C. The solutions were agitated at 1400 RPM to produce a high level of gas/liquid mass transfer by vortexing. 98% O_2/2% CO_2 at 100 ml/min is introduced across the vortexed surface of 350 ml of aqueous amine. Samples were taken at regular intervals in order to determine how degradation products over the course of the experiment. The successful experiment performed during the previous quarter was the piperazine degradation experiment; samples were sealed and stored from the previously performed MEA experiments.

With the methods reported here, glycolate still does not appear in the calibration scans. According to Lisa Lenehan, an analytical chemist with Dionex, acetate and glycolate co-elute under almost all conditions when using as AS11-HC anion column (which was the column previously being used for analysis). The recently purchased AS15 low molecular weight column is needed to separate low molecular weight organic acids efficiently. In addition to the four major organic acid degradation products (formate, acetate, glycolate, and oxalate), nitrite and nitrate are now believed to be major amine degradation products.

Figure 18 illustrates the concentration of significant degradation products from the oxidative degradation of piperazine, as determined by anion chromatography, over a 12-day experiment in the low gas flow degradation apparatus. Samples were taken at five intervals

during the course of the experiment. The most significant degradation products are formate, nitrite, and nitrate. Towards the end of the experiment, it appears that nitrite is oxidized to nitrate; if the experiment was continued for a longer period of time, nitrate and nitrite concentrations should reach steady-state concentrations. Furthermore, the formate concentration may include acetate and glycolate because the peaks appeared to be co-eluting during IC analysis.

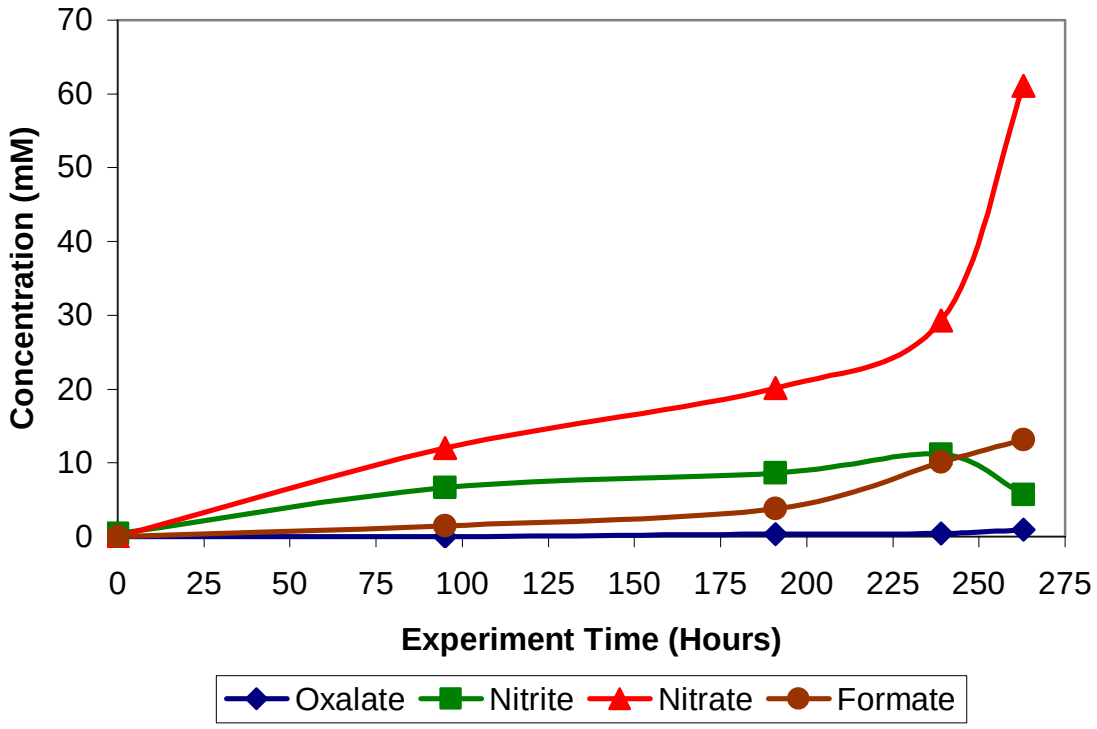

Figure 18. Oxidative degradation of 2.5 m Pz, 55°C, 1400 RPM, 350 ppm V^+, 100 ml/min 98%O_2/2%CO_2.

In addition to the November piperazine experiment, samples from the December 2004 and August 2005 MEA experiments in the low gas flow degradation apparatus were re-analyzed to determine degradation product formation rates. The August 2005 experiment was analyzed twice to check the precision of the analysis. The overall degradation rate was determined by dividing the total concentration of each product determined from the final experimental sample divided by total experiment time. The accuracy of the results from analysis of the December 2004 experiment is questionable because the samples were almost a year old; in order to obtain reliable results, it is recommended to analyze samples within a reasonable time period after they are withdrawn from the reactor. Table 10 presents a summary of degradation rates calculated from the three amine degradation experiments.

Table 10. Degradation Product Formation Rates from Oxidative Degradation of Amines in Low Gas Flow Degradation Apparatus (mM/hr).

Experiment	12/04 MEA (12 days)	09/05 MEA (14 days)	09/05 MEA (14 days)	11/05 Pz (12 days)
Analysis Date	**11/08/05**	**11/08/05**	**11/22/05**	**11/22/05**
Acetate	0.255	0.335	0.305	N/A
Formate	0.325	0.635	1.11	0.050
Oxalate	0.026	0.027	0.027	0.003
Nitrate	0.072	0.196	0.195	0.232
Nitrite	0.181	0.258	0.271	0.020

Conclusions and Future Work

Figure 18 shows that nitrate and nitrite are just as important as amine oxidative degradation products as the organic acid degradation products. Ammonia is not the only nitrogen-containing degradation product from the oxidative degradation of amines. An alternate chemistry exists by which nitrites and nitrates are formed. Therefore, it may be possible that inhibitors that reduced ammonia might not have reduced degradation rates; the inhibitor may have altered chemistry to form other nitrogen-containing degradation products. Furthermore, it appears that some type of secondary oxidation mechanism occurs that converts nitrite to nitrate, as evidenced by the depletion of nitrite and rapid increase in nitrate concentration towards the end of the piperazine degradation experiment.

Table 10 shows that the organic acid degradation products are in greater concentrations than nitrate and nitrate when MEA is subjected to oxidative degradation; on the other hand, nitrates and nitrates appear in greater concentrations than the organic acids when piperazine is degraded. Overall oxidative degradation rates appear to be lower for piperazine than for MEA. Further anion IC analysis will confirm these rates.

Cation IC analysis is moving forward as well. A method has been developed to quantify piperazine and potassium concentrations from pilot plant samples using the CS17 analytical column; this allows for the calculation of total alkalinity of the pilot plant solutions. Moreover, analysis of degraded amine samples from the low gas flow degradation apparatus suggests that ethylene diamine is a significant product from the oxidative degradation of piperazine. Further analysis is currently being conducted to confirm the presence of ethylene diamine and quantify it.

Subtask 3.1b – Analytical Methods - Total CO_2 Concentration Analysis

by Marcus Hilliard

(Supported by the Industrial Associates Program)

Reagents

Sample solutions containing 1000 ppm_v of sodium carbonate (Na_2CO_3) were obtained from Aqua Solutions without further purification. Nitrogen (N_2) gas was obtained from the Cryogenics Laboratory at The University of Texas at Austin at a purity of 99.0 mol%.

Experimental Methods

CO_2 loading analysis was determined by analyzing for total carbon dioxide by acidic evolution, 30 wt% phosphoric acid (H_2PO_4), into a Horiba PIR 2000 carbon dioxide analyzer shown in Figure 19.

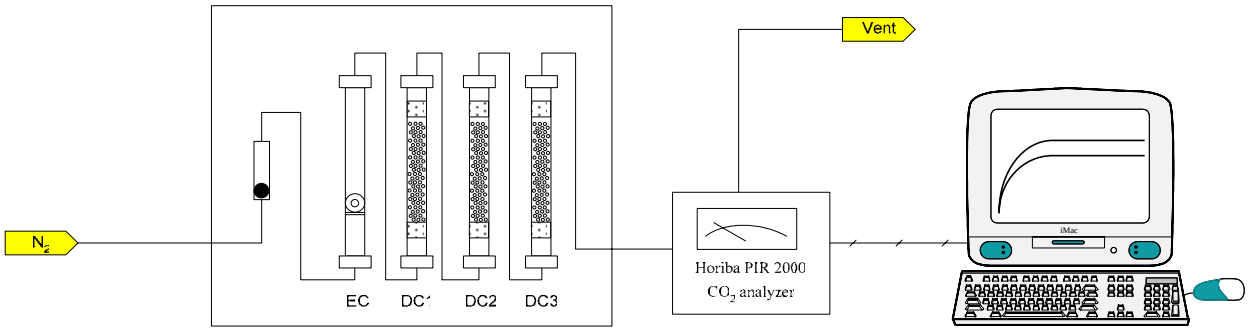

Figure 19. Process Flow Diagram for CO_2 Analysis

During the analysis, N_2 gas flows through a evolution column (EC) containing ~1 cm^3 of H_2PO_4. When a standard (1000 ppm_v Na_2CO_3) or unknown sample is injected into the EC, CO_2 is released through the following chemical reactions:

$$2H_2O \leftrightarrow H_3O^+ + OH^- \qquad Kw = \left[H_3O^+\right]\left[OH^-\right] \tag{5}$$

For the polyfunctional acid:

$$H_3PO_4 + H_2O \leftrightarrow H_2PO_4^- + H_3O^+ \qquad K_{a1}^a = \frac{\left[H_3O^+\right]\left[H_2PO_4^-\right]}{\left[H_3PO_4\right]} \tag{6}$$

$$H_2PO_4^- + H_2O \leftrightarrow HPO_4^{2-} + H_3O^+ \qquad K_{a2}^a = \frac{\left[H_3O^+\right]\left[HPO_4^{2-}\right]}{\left[H_2PO_4^-\right]} \tag{7}$$

$$HPO_4^{2-} + H_2O \leftrightarrow PO_4^{3-} + H_3O^+ \qquad \mathrm{K_{a3}^a} = \frac{\left[H_3O^+\right]\left[PO_4^{3-}\right]}{\left[HPO_4^{2-}\right]} \tag{8}$$

For the polyfunctional base:

$$HCO_3^- + H_2O \leftrightarrow H_3O^+ + CO_3^{2-} \qquad \mathrm{K_{a1}^b} = \frac{\left[H_3O^+\right]\left[CO_3^{2-}\right]}{\left[HCO_3^-\right]} \tag{9}$$

$$H_2CO_3 + H_2O \leftrightarrow H_3O^+ + HCO_3^- \qquad \mathrm{K_{a2}^b} = \frac{\left[H_3O^+\right]\left[HCO_3^-\right]}{\left[H_2CO_3\right]} \tag{10}$$

$$H_2CO_3(aq) \rightarrow H_2O(l) + CO_2(aq) \tag{11}$$

Since Equation 11 lies far to the right, we can substitute Equation 11 into Equation 10.

$$CO_2(aq) + 2H_2O \leftrightarrow H_3O^+ + HCO_3^- \qquad \mathrm{K_{a2}^b} = \frac{\left[H_3O^+\right]\left[HCO_3^-\right]}{\left[CO_2\right]} \tag{12}$$

The pH of polyfunctional systems can be computed rigorously through a systematic multiple-equilibrium approach which describes the concentration of these species in solution:

Mass-Balance Expressions

For the Base:

$$c_{Na_2CO_3} = \frac{1}{2}\left[Na^{+1}\right] + \left[CO_3^{-2}\right] + \left[HCO_3^-\right] + \left[CO_2\right] \tag{13}$$

Alternatively: If the only source of Na^+, CO_3^{2-}, HCO_3^-, and CO_2 is Na_2CO_3, then Equation 13 can be rewritten as:

$$c_{Na_2CO_3} = \frac{1}{2}\left[Na^{+1}\right] = \left[CO_3^{-2}\right] + \left[HCO_3^-\right] + \left[CO_2\right] \tag{14}$$

For the Acid:

$$c_{H_3PO_4} = \left[H_3PO_4\right] + \left[H_2PO_4^-\right] + \left[HPO_4^{2-}\right] + \left[PO_4^{3-}\right] \tag{15}$$

Charge-Balance Expression

$$\left[Na^+\right] + \left[H_3O^+\right] = \left[OH^-\right] + \left[H_2PO_4^-\right] + 2\left[HPO_4^{2-}\right] + 3\left[PO_4^{3-}\right] + 2\left[CO_3^{2-}\right] + \left[HCO_3^-\right]$$

(16)

The changes in composition that occur in a solution of a polyfunctional acid and base can be visualized by the relative concentrations called alpha values. If we let c_i be the sum of the molar concentrations of the acidic and basic containing species in the solution throughout the titration, the alpha value for the free acid, α_0, and free base, α_4, is defined as

$$\alpha_0 = \frac{\left[H_3PO_4\right]}{c_{H_3PO_4}} \tag{17}$$

$$\alpha_4 = \frac{\left[CO_3^-\right]}{c_{Na_2CO_3}} \tag{18}$$

where $c_{H_3PO_4}$ and $c_{Na_2CO_3}$ are defined by Equation 13 and 14, respectively. The alpha values for the other species are given by similar equations:

$$\alpha_1 = \frac{\left[H_2PO_4^-\right]}{c_{H_3PO_4}} \tag{19}$$

$$\alpha_2 = \frac{\left[HPO_4^{2-}\right]}{c_{H_3PO_4}} \tag{20}$$

$$\alpha_3 = \frac{\left[PO_4^{3-}\right]}{c_{H_3PO_4}} \tag{21}$$

$$\alpha_5 = \frac{\left[HCO_3^{-}\right]}{c_{Na_2CO_3}} \tag{22}$$

$$\alpha_6 = \frac{\left[CO_2\right]}{c_{Na_2CO_3}} \tag{23}$$

where the sum of the alpha values for each system must equal unity. That is,

$$\alpha_0 + \alpha_1 + \alpha_2 + \alpha_3 = 1 \tag{24}$$

and

$$\alpha_4 + \alpha_5 + \alpha_6 = 1 \tag{25}$$

Alpha values are determined by $\left[H_3O^+\right]$ and K_{ai} alone. To obtain an expression for α_0, we rearrange Equation 6 to

$$\left[H_2PO_4^{-}\right] = \frac{\mathrm{K}_{\mathrm{a1}}^{\mathrm{a}}\left[H_3PO_4\right]}{\left[H_3O^+\right]} \tag{26}$$

$$\left[HPO_4^{2-}\right] = \frac{\mathrm{K}_{\mathrm{a2}}^{\mathrm{a}}\left[H_2PO_4^{-}\right]}{\left[H_3O^+\right]} \tag{27}$$

$$\left[PO_4^{3-}\right] = \frac{\mathrm{K}_{\mathrm{a3}}^{\mathrm{a}}\left[HPO_4^{2-}\right]}{\left[H_3O^+\right]} \tag{28}$$

Substituting the previous equations in to Equation 15 gives

$$c_{H_3PO_4} = \left[H_3PO_4\right] + \frac{\mathrm{K}_{a1}^{a}\left[H_3PO_4\right]}{\left[H_3O^+\right]} + \frac{\mathrm{K}_{a2}^{a}\left(\frac{\mathrm{K}_{a1}^{a}\left[H_3PO_4\right]}{\left[H_3O^+\right]}\right)}{\left[H_3O^+\right]} + \frac{\mathrm{K}_{a3}^{a}\left(\frac{\mathrm{K}_{a2}^{a}\left(\frac{\mathrm{K}_{a1}^{a}\left[H_3PO_4\right]}{\left[H_3O^+\right]}\right)}{\left[H_3O^+\right]}\right)}{\left[H_3O^+\right]}$$

(29)

Upon rearrangement we obtain

$$c_{H_3PO_4} = \left[H_3PO_4\right]\left(\frac{\left[H_3O^+\right]^3 + \left[H_3O^+\right]^2 K_{a1}^{a} + \left[H_3O^+\right]K_{a1}^{a}K_{a2}^{a} + K_{a1}^{a}K_{a2}^{a}K_{a3}^{a}}{\left[H_3O^+\right]^3}\right) \quad (30)$$

$$\frac{c_{H_3PO_4}}{\left[H_3PO_4\right]} = \frac{\left[H_3O^+\right]^3 + \left[H_3O^+\right]^2 K_{a1}^{a} + \left[H_3O^+\right]K_{a1}^{a}K_{a2}^{a} + K_{a1}^{a}K_{a2}^{a}K_{a3}^{a}}{\left[H_3O^+\right]^3} \quad (31)$$

Substituting Equation 17 into Equation 31 yields,

$$\alpha_0 = \frac{\left[H_3PO_4\right]}{c_{H_3PO_4}} = \frac{\left[H_3O^+\right]^3}{\left[H_3O^+\right]^3 + \left[H_3O^+\right]^2 K_{a1}^{a} + \left[H_3O^+\right]K_{a1}^{a}K_{a2}^{a} + K_{a1}^{a}K_{a2}^{a}K_{a3}^{a}} \quad (32)$$

The alpha values for the other acidic species are given by similar equations:

$$\alpha_1 = \frac{\left[H_2PO_4^-\right]}{c_{H_3PO_4}} = \frac{\left[H_3O^+\right]^2 K_{a1}^{a}}{\left[H_3O^+\right]^3 + \left[H_3O^+\right]^2 K_{a1}^{a} + \left[H_3O^+\right]K_{a1}^{a}K_{a2}^{a} + K_{a1}^{a}K_{a2}^{a}K_{a3}^{a}} \quad (33)$$

$$\alpha_2 = \frac{\left[HPO_4^{2-}\right]}{c_{H_3PO_4}} = \frac{\left[H_3O^+\right]K_{a1}^{a}K_{a2}^{a}}{\left[H_3O^+\right]^3 + \left[H_3O^+\right]^2 K_{a1}^{a} + \left[H_3O^+\right]K_{a1}^{a}K_{a2}^{a} + K_{a1}^{a}K_{a2}^{a}K_{a3}^{a}} \quad (34)$$

$$\alpha_3 = \frac{\left[PO_4^{3-}\right]}{c_{H_3PO_4}} = \frac{K_{a1}^a K_{a2}^a K_{a3}^a}{\left[H_3O^+\right]^3 + \left[H_3O^+\right]^2 K_{a1}^a + \left[H_3O^+\right] K_{a1}^a K_{a2}^a + K_{a1}^a K_{a2}^a K_{a3}^a} \tag{35}$$

Similarly, the alpha values for the basic species are given as

$$\left[HCO_3^-\right] = \frac{\left[H_3O^+\right]\left[CO_3^{2-}\right]}{\mathrm{K}_{a1}^b} \tag{36}$$

$$\left[CO_2\right] = \frac{\left[H_3O^+\right]\left[HCO_3^-\right]}{\mathrm{K}_{a2}^b} \tag{37}$$

Substituting the previous equations in to Equation 14 gives

$$c_{Na_2CO_3} = \left[CO_3^{-2}\right] + \frac{\left[H_3O^+\right]\left[CO_3^{2-}\right]}{\mathrm{K}_{a1}^b} + \frac{\left[H_3O^+\right]\left(\frac{\left[H_3O^+\right]\left[CO_3^{2-}\right]}{\mathrm{K}_{a1}^b}\right)}{\mathrm{K}_{a2}^b} \tag{38}$$

Upon rearrangement we obtain

$$c_{Na_2CO_3} = \left[CO_3^{-2}\right] + \frac{\left[H_3O^+\right]\left[CO_3^{2-}\right]}{\mathrm{K}_{a1}^b} + \frac{\left[H_3O^+\right]^2\left[CO_3^{2-}\right]}{\mathrm{K}_{a1}^b \mathrm{K}_{a2}^b} \tag{39}$$

$$c_{Na_2CO_3} = \left[CO_3^{-2}\right]\left(\frac{\left[H_3O^+\right]^2 + \left[H_3O^+\right]\mathrm{K}_{a2}^b + \mathrm{K}_{a1}^b \mathrm{K}_{a2}^b}{\mathrm{K}_{a1}^b \mathrm{K}_{a2}^b}\right) \tag{40}$$

Substituting Equation 18 into Equation 40 yields,

$$\alpha_4 = \frac{\left[CO_3^{-2}\right]}{c_{Na_2CO_3}} = \frac{\mathrm{K}_{a1}^b \mathrm{K}_{a2}^b}{\left[H_3O^+\right]^2 + \left[H_3O^+\right]\mathrm{K}_{a2}^b + \mathrm{K}_{a1}^b \mathrm{K}_{a2}^b} \tag{41}$$

$$\alpha_5 = \frac{\left[HCO_3^-\right]}{c_{Na_2CO_3}} = \frac{\left[H_3O^+\right]\mathrm{K}_{a2}^{b}}{\left[H_3O^+\right]^2 + \left[H_3O^+\right]\mathrm{K}_{a2}^{b} + \mathrm{K}_{a1}^{b}\mathrm{K}_{a2}^{b}} \tag{42}$$

$$\alpha_6 = \frac{\left[CO_2\right]}{c_{Na_2CO_3}} = \frac{\left[H_3O^+\right]^2}{\left[H_3O^+\right]^2 + \left[H_3O^+\right]\mathrm{K}_{a2}^{b} + \mathrm{K}_{a1}^{b}\mathrm{K}_{a2}^{b}} \tag{43}$$

Substituting the above unknowns alpha values into the charge-balance expression (Equation 16)

$$\left[Na^+\right] + \left[H_3O^+\right] = \left[OH^-\right] + \left[H_2PO_4^-\right] + 2\left[HPO_4^{2-}\right] + 3\left[PO_4^{3-}\right] + 2\left[CO_3^{2-}\right] + \left[HCO_3^-\right]$$

which yields,

$$2c_{Na_2CO_3} + \left[H_3O^+\right] = \frac{K_w}{\left[H_3O^+\right]} + c_{H_3PO_4}\alpha_1 + 2\left(c_{H_3PO_4}\alpha_2\right) + 3\left(c_{H_3PO_4}\alpha_3\right) + 2\left(c_{Na_2CO_3}\alpha_4\right) + c_{Na_2CO_3}\alpha_5 \tag{44}$$

$$2c_{Na_2CO_3}+\left[H_3O^+\right]=\frac{K_w}{\left[H_3O^+\right]}+c_{H_3PO_4}\left(\frac{\left[H_3O^+\right]^2K_{a1}^a}{\left[H_3O^+\right]^3+\left[H_3O^+\right]^2K_{a1}^a+\left[H_3O^+\right]K_{a1}^aK_{a2}^a+K_{a1}^aK_{a2}^aK_{a3}^a}\right)$$
$$+2\left(c_{H_3PO_4}\left(\frac{\left[H_3O^+\right]K_{a1}^aK_{a2}^a}{\left[H_3O^+\right]^3+\left[H_3O^+\right]^2K_{a1}^a+\left[H_3O^+\right]K_{a1}^aK_{a2}^a+K_{a1}^aK_{a2}^aK_{a3}^a}\right)\right)$$
$$+3\left(c_{H_3PO_4}\left(\frac{K_{a1}^aK_{a2}^aK_{a3}^a}{\left[H_3O^+\right]^3+\left[H_3O^+\right]^2K_{a1}^a+\left[H_3O^+\right]K_{a1}^aK_{a2}^a+K_{a1}^aK_{a2}^aK_{a3}^a}\right)\right)$$
$$+2\left(c_{Na_2CO_3}\left(\frac{\mathrm{K_{a1}^bK_{a2}^b}}{\left[H_3O^+\right]^2+\left[H_3O^+\right]\mathrm{K_{a2}^b}+\mathrm{K_{a1}^bK_{a2}^b}}\right)\right)$$
$$+c_{Na_2CO_3}\left(\frac{\left[H_3O^+\right]\mathrm{K_{a2}^b}}{\left[H_3O^+\right]^2+\left[H_3O^+\right]\mathrm{K_{a2}^b}+\mathrm{K_{a1}^bK_{a2}^b}}\right)$$

(45)

We can now solve the above equation for the $\left[H_3O^+\right]$ power series…

$$\left[H_3O^+\right]^7+\left[H_3O^+\right]^6\left(K_{a1}^a+K_{a2}^b+2c_{Na_2CO_3}\right)-\left[H_3O^+\right]^5\begin{pmatrix}c_{H_3PO_4}K_{a1}^a-K_{a1}^a\left(K_{a2}^a+K_{a2}^b+2c_{Na_2CO_3}\right)\\-K_{a1}^bK_{a2}^b-K_{a2}^bc_{Na_2CO_3}+K_w\end{pmatrix}$$
$$-\left[H_3O^+\right]^4\begin{pmatrix}c_{H_3PO_4}K_{a1}^a\left(2K_{a2}^a+K_{a2}^b\right)-K_{a1}^a\begin{pmatrix}K_{a1}^bK_{a2}^b+K_{a2}^a\left(K_{a2}^b+K_{a3}^a+2c_{Na_2CO_3}\right)\\+K_{a2}^bc_{Na_2CO_3}-K_w\end{pmatrix}\\+K_{a2}^bK_w\end{pmatrix}$$
$$-\left[H_3O^+\right]^3\begin{pmatrix}c_{H_3PO_4}K_{a1}^a\left(K_{a1}^bK_{a2}^b+K_{a2}^a\left(2K_{a2}^b+3K_{a3}^a\right)\right)\\-K_{a1}^a\begin{pmatrix}K_{a1}^bK_{a2}^aK_{a2}^b+K_{a2}^a\begin{pmatrix}K_{a2}^b\left(K_{a3}^a+c_{Na_2CO_3}\right)\\+2K_{a3}^ac_{Na_2CO_3}-K_w\end{pmatrix}\\-K_{a2}^bK_w\end{pmatrix}\\+K_{a1}^bK_{a2}^bK_w\end{pmatrix}$$
$$-\left[H_3O^+\right]^2\begin{pmatrix}c_{H_3PO_4}\left(2K_{a1}^b+3K_{a3}^a\right)K_{a2}^aK_{a2}^b-K_{a1}^b\left(K_{a2}^aK_{a3}^a-K_w\right)K_{a2}^b\\-K_{a2}^a\begin{pmatrix}K_{a2}^b\left(K_{a3}^ac_{Na_2CO_3}-K_w\right)\\-K_{a3}^aK_w\end{pmatrix}\end{pmatrix}K_{a1}^a$$
$$-\left[H_3O^+\right]\left(3c_{H_3PO_4}K_{a1}^bK_{a3}^a+\left(K_{a1}^b+K_{a3}^a\right)K_w\right)K_{a1}^aK_{a2}^aK_{a2}^b$$
$$-K_{a1}^aK_{a1}^bK_{a2}^aK_{a2}^bK_{a3}^aK_w=0 \tag{46}$$

Though difficult, the above equation can be used to solve for the molar $\left[H_3O^+\right]$ using known values for the equilibrium constants and the formal concentrations of the acid and base in the solution that is being titrated. The concentration of the acid/base can be described during the dilution as

$$c_{H_3PO_4}=\frac{V_{tit}c_{H3PO4}^o}{V_{tit}+V_{anal}} \tag{47}$$

$$c_{Na_2CO_3}=\frac{V_{anal}c_{Na_2CO_3}^o}{V_{tit}+V_{anal}} \tag{48}$$

where,

V_{tit} and V_{anal} are the titrant and analyte solution volumes, respectively,

$c^{o}_{H_3PO_4}$ and $c^{o}_{Na_2CO_3}$ are the initial acid and base molar concentrations.

For example, Figure 20 shows the partial titration curve of 1 ml of 30 wt% of H_3PO_4 with 1000 ppm_v of Na_2CO_3. Equilibrium constants were obtained from Martell *et al.* (1989) at 25°C as given in Table 11.

Table 11. Equilibrium constants evaluated at 25 °C.

Acid	25 °C
K_{a1}	7.11E-03
K_{a2}	6.32E-08
K_{a3}	4.50E-13

Base	25 °C
K_{a1}	4.45E-07
K_{a2}	4.69E-11

H_2O	25 °C
K_w	1.00E-14

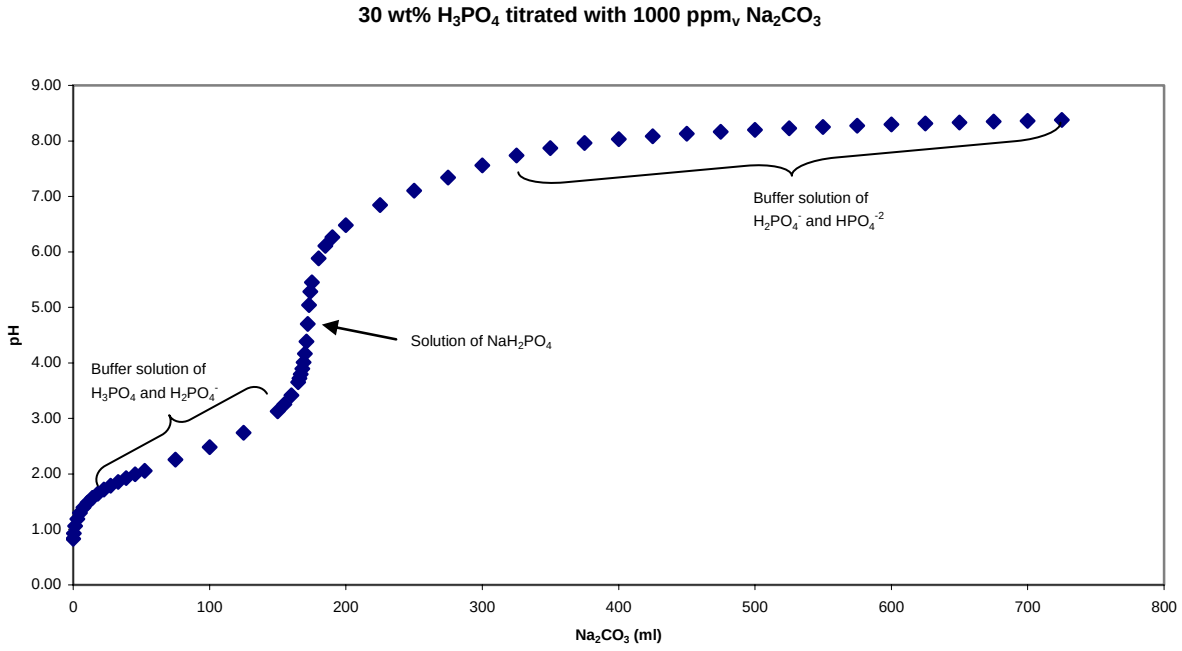

Figure 20. Titration of 1 ml of 30 wt% H_3PO_4 with 1000 ppm_v of Na_2CO_3.

The volume of the evolution column is ~3 ml. The volume of Na_2CO_3 injected into the evolution column during the calibration is ~1.5 ml where the pH of the solution is 1.06. This would leave enough volume for five 0.1 ml injections of an unknown sample into the evolution column. Thus, the only limiting factor for the evolution of CO_2 during this titration is the capacity of the evolution column due to the acidic nature of the solution, as shown in Figure 21.

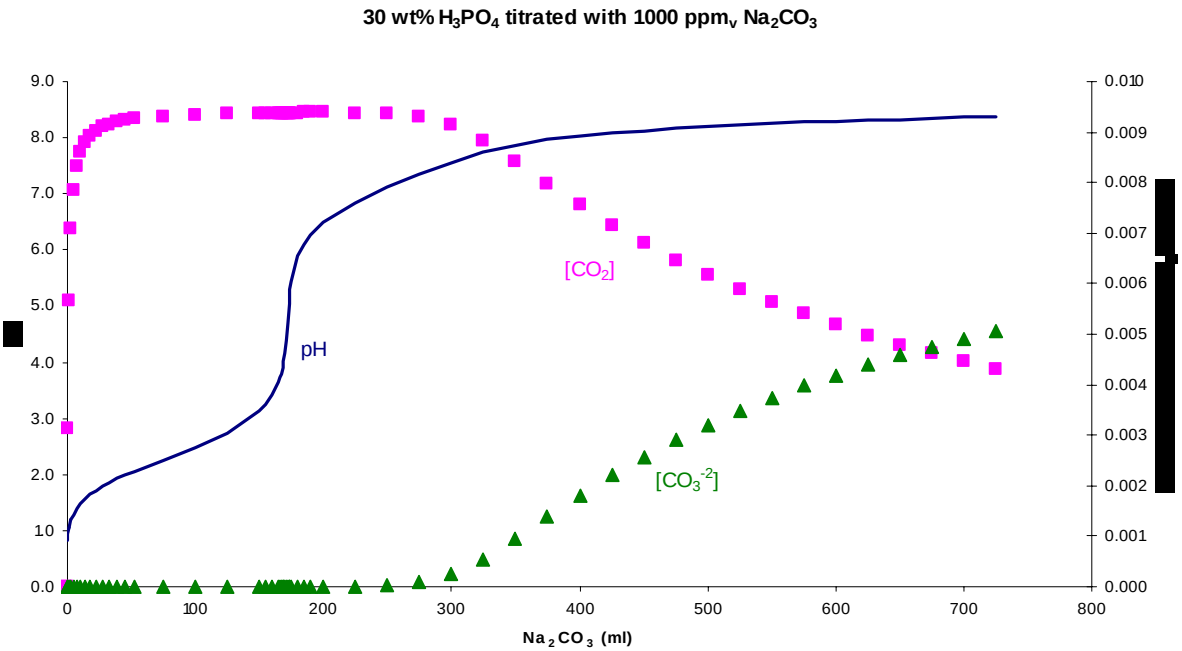

Figure 21. Molar concentration curves of CO_2 species during the titration of 1 ml of 30 wt% H_3PO_4 with 1000 ppm_v of Na_2CO_3.

Standard operating procedure for CO_2 analysis

Sample Preparation

For each sample to be analyzed, the total CO_2 concentration (carbonate, bicarbonate, and carbon dioxide) in each sample should be within the range of 0.47 – 1.89 μmole of total CO_2. If the sample has a high total CO_2 concentration, the sample should be diluted in order for the analyzer response to stay within the calibration range.

Sample Dilution

1. Weigh a dry 25 ml volumetric flask and tare the scale.
2. Use an automatic pipette; dispense 100 μl of your sample into the volumetric flask.
3. Record the weight of the sample and tare the scale.
4. Use a glass pipette and dispense ~25 ml of Ultra pure DI-water so that the meniscus or the curved upper surface of the liquid is just touching the 25 ml calibration line.
5. Record the weight of the sample.
6. Seal the volumetric flask with a yellow stopper.
7. Use the following formula to calculate the concentration of your new sample

$$\frac{C_1^{Con}\left(\frac{mole}{kg-sol}\right)V_1^{Con}\left(kg-sol\right)}{V_2^{Dil}\left(kg-sol\right)} = C_2^{Dil}\left(\frac{mole}{kg-sol}\right)$$

where,

C_1^{Con} is the total CO_2 concentration of your sample, $\left[\frac{mole}{kg-sol}\right]$,

V_1^{Con} is the weight of the 100 µl of your sample, $[kg]$,

V_2^{Dil} is the weight of ~25 ml of Ultra pure DI-water plus V_1^{Con}, $[kg]$.

This method will dilute your sample by a factor of $100\left(V_2^{Dil}/V_1^{Con}\right)$. Use the following formula to check if the total CO_2 concentration of your dilute sample is within the range of 0.47 – 1.89 µmole of total CO_2.

$$n_{CO_2}^{Dil}[\mu mole] = C_2^{Dil}\left(\frac{(mole)}{kg-sol}\right)\cdot 0.1$$

Equipment Preparation

Drying bed(s)

There are 3 magnesium perchlorate drying beds on the carbonate analyzer. The first bed must be changed each day before analyzing samples. It may also need to be changed again if many samples are to be analyzed. The second drying bed may be changed occasionally if the analyzer continues giving erratic results after changing the first bed. The third drying bed should rarely need to be changed.

To change any of the drying beds:

1. Remove the drying bed by pulling up on the glass tube. Be careful not to break the glass.
2. Discard the glass wool and the old bed.
3. Wash out the glass tube and then dry thoroughly.
4. Cut a small piece of glass wool and insert it into one end of the glass tube.
5. Through the other end, fill the tube with large magnesium perchlorate crystals.
6. Cut another small piece of glass wool and insert it into the open end of the tube.
7. Place the drying bed back in the carbonate analyzer.

Gas flow

1. Verify that the nitrogen (N_2) cylinder is open and the pressure regulator is set at a minimum pressure of 40 psi.
2. Open the nitrogen needle valve by the hood.
3. Adjust the rotameter so that the middle of the ball float is at 12.
4. Check that the gas is flowing all the way through the analyzer and is not obstructed.
5. Allow N_2 to flow through the analyzer for ~5 minutes before starting your analysis.

Acid bath

1. Obtain 30 wt% phosphoric acid (H_3PO_4) solution.
2. Check the septum on the analyzer for wear. If necessary, turn off gas and replace septum.
3. Using a 3mL syringe, inject approximately 1mL of acid into the analyzer.
4. Wait for the background CO_2 to be stripped out of solution and allow the analyzer response to stabilize/return back to "zero."

Data Logger

1. Turn on the computer and log-in using the Rochelle Group password.
2. The data logger software can be found by going to START>Programs>Pico Technology>PicoLog Recorder
3. The data logger will record the voltage, in 1 second increments, from the CO_2 analyzer and display the values graphically and in a tabular spreadsheet format.
4. Create a new file for your calibration/sample data points by pressing the **New File** button on the control panel.
5. Save your data under My Documents and then the appropriate subfolder.
    a. 264 groups have their own folder and subfolders where students can save their work during the semester. This folder will be purged at the end of term.
6. When you are ready to start collecting data, **BEFORE** you inject a solution into the CO_2 analyzer, press the **Start Recording** button on the control panel.
7. When you are finished collecting data for sample, press the **Stop Recording** button on the control panel.
8. You can transfer your tabular data to Excel by pressing Select button and then by pressing Copy to clipboard button on the control panel.
9. Open Excel and select cell A1 and press Ctrl V to paste your data into the spreadsheet.
10. Make sure that the average area deviation for each group of calibration points is < 2 % error. Please refer to the Data Analysis Section for more information about calculating the area for each curve.

Calibration

The calibration solutions and procedure will depend on the expected concentrations of the samples to be analyzed.

Standard solutions

For our standard, we will be using a 1000 ppm_v solution of sodium carbonate (Na_2CO_3) obtained from Aqua Solutions. Make sure that you follow proper laboratory procedures when handling this standard. *Please replace and tighten the cap after each use*.

Calibration procedure

Calibrate the total carbonate analyzer by injecting different amounts of a known concentration.

1. Adjust the range on the analyzer. (For spray experiments, the analyzer should be on the 0.05% range.)

2. Flush a 250 µL syringe with Ultra-pure DI-H_2O and discard into a waste container.
3. Repeat Step 2 three times to clean the syringe.
4. Record the weight of the syringe.
5. Draw 50 µL of standard solution into a 250µL syringe and then discard it.
6. Draw 50µL of standard solution into the 250µL syringe.
7. Record the weight of the syringe.
8. Press Start Recording on the Data Logger control panel.
9. Inject the 50µL of standard solution into the analyzer.
10. Watch for the peak on the data logger and wait for the analyzer output to return to zero.
11. Repeat steps 2, 3, 5-7, 9-10 until you have three peaks in close agreement (similar peak heights).
12. Press Stop Recording when you are finished collecting data for a particular data point.
13. Press Re-Record and then create a new file to store your new data.
14. Repeat with other volumes of standard solution (100, 150, and 200µL) to create a calibration curve.

Sample Analysis

1. Flush a 250 µL syringe with Ultra-pure DI-H_2O and discard into a waste container.
2. Repeat Step 2 three times to clean the syringe.
3. Record the weight of the syringe.
4. Draw 100µL of the dilute sample into the 250µL syringe and then discard it.
5. Draw 100µL of the dilute sample into the 250µL syringe.
6. Record the weight of the syringe.
7. Press Start Recording on the Data Logger control panel.
8. Inject the 100µL of sample into the analyzer.
9. Watch for the peak on the data logger and wait for the analyzer output to return to zero.
10. Repeat steps 1-9 until you have three peaks in close agreement (similar peak heights).
11. Press Stop Recording when you are finished collecting data for a particular data point.

Data Analysis

Once you have collected your data, integrate the peak area using the trapezoid rule.

$$A = \sum_{i=1}^{n} a_i = \frac{h}{2} \sum_{i=1}^{n} \left(f_i + f_{i+1} \right)$$

where,

n is the number of data points in your curve,

h is the length of the interval, 1 sec,

f_i is the voltage of data point *i*.

In Excel, your data should look something like this.

	A	B	C
1	Sample	1	
2	Time	Voltage	Area
3	Seconds	V	
4			Trapezoid
5	0	0	=(B5+B6)*0.5
6	1	0.0027	=(B6+B7)*0.5+C5
7	2	0.0098	=(B6+B7)*0.5+C6

Drag the formula in cell C7 until the analyzer output (voltage) returns to zero. At this point, the value will correspond to the area under the curve.

1. Calculate the area for the other data points you have collected.
2. Calculate the average area for each set of data points.
3. Make sure that the average area deviation for each group of calibration points is < 2 % error.

Your results will look something like this.

Calibration Results

Syringe (gm) 12.9734

	Assumed		Actual					
Obs	Volume (μl)	CO_2^{tot} (μmole)	Weight (gm)	CO_2^{tot} (μmole)	Area V^2	Ave Area V^2	STDEV	Error %
1	50	0.4717	13.0260	0.4968	1.2779	1.2547	0.0256	1.85
2	50	0.4717	13.0281	0.5167	1.2273			2.18
3	50	0.4717	13.0269	0.5053	1.2589			0.33
1	100	0.9435	13.0767	0.9757	2.9187	2.9304	0.0189	0.40
2	100	0.9435	13.0772	0.9804	2.9522			0.74
3	100	0.9435	13.0822	1.0276	2.9204			0.34
1	150	1.4152	13.1280	1.4602	4.4147	4.4328	0.0161	0.41
2	150	1.4152	13.1301	1.4801	4.4456			0.29
3	150	1.4152	13.1275	1.4555	4.4381			0.12
1	200	1.8870	13.1748	1.9023	5.7177	5.7518	0.0306	0.59
2	200	1.8870	13.1834	1.9835	5.7606			0.15
3	200	1.8870	13.1860	2.0081	5.7770			0.44

Create a correlation between the peak area and the total CO_2 concentration $(\mu mole)$. From this you will be able to determine the total CO_2 concentration of your unknown sample.

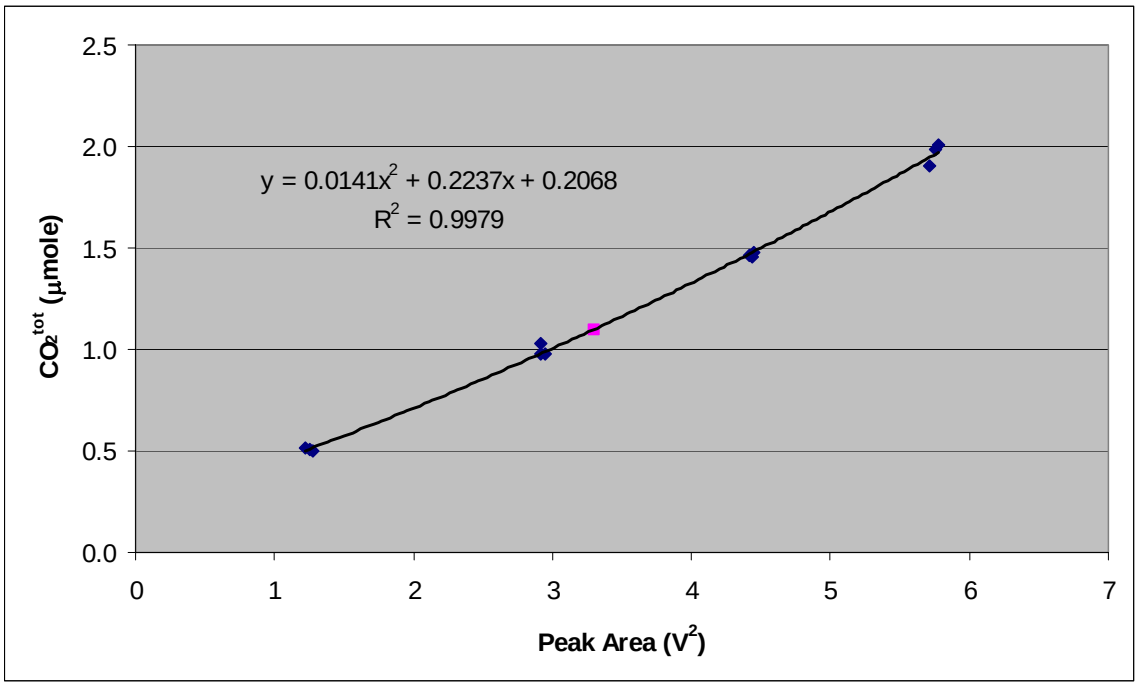

Troubleshooting

From time to time, check that the rotameter is still at 12 and inject 100µL of standard solution to check the calibration.

Sample cell gets full

1. Remove the acid bath/sample solution from the analyzer with the 3mL syringe.
2. Flush a 250 µL syringe with Ultra-pure DI-H_2O and discard into a waste container.
3. Using a 3mL syringe, inject approximately 1mL of acid into the analyzer.
4. Wait for the background CO_2 to be stripped out of solution. Allow the analyzer response to stabilize/return back to "zero."
5. Inject 100µL of standard solution to check the calibration.

Sudden drop in gas flow

1. Check gas flow through analyzer.
2. May need to change the drying bed. Turn off the gas flow, empty the acid bath, and replace the drying bed(s).

No response from analyzer

1. Check gas flow through analyzer.
2. Inspect tubing inside and outside of analyzer.

Shutdown

1. Reduce the gas flow by turning the rotameter down to about 3.
2. Remove the acid bath/sample solution from the analyzer with the 3mL syringe.
3. Turn the rotameter down to zero. Close the nitrogen needle valve by the hood.

4. If no one else is using the nitrogen, close the cylinder.
5. Rinse the syringes with distilled water.
6. Close the PicoLog Recorder and shut down the computer.

Error Analysis

Error in sample preparation

The accuracy of the scale used for weighing syringes and solution preparation was ± 0.0002 gm. The error in the specified number of moles of species in the sample was then evaluated using an error propagation formula. The average uncertainty in the number of micromoles of sodium carbonate injected into the Horiba PIR 2000 carbon dioxide analyzer was ± 0.0030 μmole with a maximum uncertainty of ± 0.0034 μmole.

If the injections were done on a volume basis, the average absolute relative error was 4.80 % and the maximum absolute relative error was 8.69 %. Possible causes for this discrepancy may include: air bubbles within the syringe, improper handling of the syringe, and human error associated with small-volume solutions conditions.

From the above results, we can calculate the uncertainty within the correlation between the peak area and the total CO_2 concentration using the two methods of injection i.e. mass and volume. The absolute relative error and the standard error of the measurement associated with the two methods are shown in Table 12.

Table 12. Peak Area as compared to mass and volume injections.

Solution	Peak Area				E - PAV
	Mass	σ^{Mass}	Volume	σ^{Volume}	(%)
1-1	1.10	0.03	1.052	0.008	4.22
1-2	1.52	0.03	1.457	0.008	3.86
1-3	1.67	0.03	1.602	0.008	3.84

Previous researchers developed correlations between peak height and the total CO_2 concentration with the assumption that the peak height was proportional to the peak area. If injections were preformed on a mass or volume basis, the average absolute relative error was 2.19% and 6.13%, respectively, as compared to a mass injection associated with the peak area, shown in Table 13.

Table 13. Comparison between Peak Area versus Peak Height.

Solution	Peak Area		Peak Height				E - PHM	E - PHV
	Mass	σ^{Mass}	Mass	σ^{Mass}	Volume	σ^{Volume}	(%)	(%)
1-1	1.10	0.03	1.08	0.05	1.03	0.04	1.82	6.05
1-2	1.52	0.03	1.50	0.05	1.44	0.04	1.25	5.12
1-3	1.67	0.03	1.61	0.05	1.55	0.04	3.49	7.22

From the above analysis, we could conclude that previous results for total CO_2 concentration may have been under estimated on the order of 6.13 %. It is then recommended that future CO_2 analysis should be based on the peak area with mass injections.

Subtask 3.4 – Amine Volatility

by John McLees and Marcus Hilliard
(Supported by this contract)

Introduction

The main focus of this subtask is to present initial partial pressure and calculated activity coefficient results for H_2O, MEA-H_2O, and PZ-H_2O systems generated in a stirred reactor. These three systems were each allowed to equilibrate at temperatures from 40-70 ^oC. The gas compositions were measured using a Fourier-Transform infrared (FTIR) analyzer at 180^oC. The experimental results for the MEA-H_2O system were compared to predictions generated in Aspen Plus using the NRTL parameters for the amine-water systems developed by Posey (1994) while the results for the PZ-H_2O systems were compared to predictions by the UNIFAC-Dortmund Modified (DMD) model (Gmehling *et al*., 1993) in Aspen Plus.

Experimental Methods

FTIR Analysis with Stirred Reactor

For this work, the tests were conducted on an existing stirred reactor setup in the laboratory. Prior to testing amine-water solutions, two baseline water experiments were run in the apparatus to quantify the amount of error that may be present. The amine-water solutions were prepared on a mass basis by weighing out a pre-determined amount of water and adding the correct mass of amine. For these tests, 7m MEA and 2.5m PZ solutions were used.

Sample solutions containing the MEA, PZ, and ultra pure deionized water (H_2O) were prepared from Acros Organics, Flucka, and the Department of Chemical Engineering at The University of Texas at Austin, respectively, without further purification. CO_2 and nitrogen (N_2) gases were obtained from Matheson Tri-Gas and the Cryogenics Laboratory at The University of Texas at Austin at a purity of 99.5 mol% and 99.0 mol%, respectively.

Partial pressures of vapor phase components were determined using a vapor-liquid equilibrium apparatus with recirculation of the gas phase as shown in Figure 22. The apparatus was designed to operate at atmospheric pressure and temperatures up to 100^oC.

During an experiment, a 1000 cm^3 glass stirred reactor is filled with a known amount of sample solution to a volume of approximately 500 cm^3. The reactor is located within a thermostated cylinder where the temperature of the reactor will be measured within ± 0.1 ^oC and controlled through the use of a water bath. When the experimental temperature is reached, the wet vapor phase is then allowed to circulate, where the vapor stream passes into a heated sample line operated at approximately 180 ^oC before entering a Temet GasmetTM DX-Series portable Fourier-Transform infrared spectrometer. The vapor stream is then analyzed to determine the volume percent of water and amine present. After analysis, the vapor stream is then circulated back to the reactor through a second heated line operating at approximately 100 ^oC. Equilibrium is obtained when the temperature and the H_2O concentration in the vapor phase are constant.

Once the data was collected at 40 ^oC, this process was repeated at 50 and 70 ^oC, respectively, using the same liquid solution. At the conclusion of the test, the liquid solution was re-weighed to account for any lost mass, and the results were tabulated.

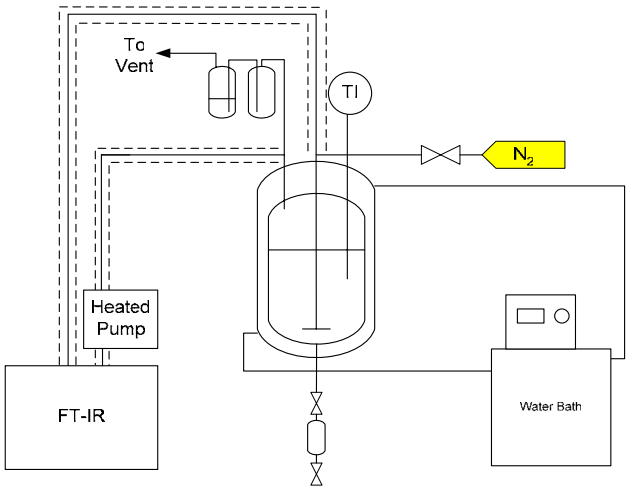

Figure 22. Process Flow Diagram for Vapor Phase Speciation Experiments

Results and Discussion

aH_2O Benchmark Experiment

Tests were conducted in the stirred reactor system using ultra-pure deionized water as an initial baseline to assess the amount of error in the experimental method. Water was tested on two separate dates (12/14 and 12/20/05) and the results are tabulated in Table 14.

Table 14. Experimental Results for H_2O via FTIR Analysis.

Date	Obs	Temp (^oC)	y_{H2O}	PT (kPa)	P_{H2O}^{exp} (kPa)	P_{H2O}^{act} (kPa)	Error (%)	Exp/Est
12/14/2005	1	32.1	0.0424	116.5	4.9	4.8	3.14	1.031
12/14/2005	2	50.8	0.1137	116.9	13.3	12.9	3.24	1.032
12/14/2005	3	68.3	0.2503	116.3	29.1	28.9	0.66	1.007
12/20/2005	4	34.8	0.050	118.0	5.9	5.6	5.89	1.059
12/20/2005	5	49.6	0.1076	118.1	12.7	12.1	4.76	1.048
12/20/2005	6	70.7	0.2672	115.4	30.8	32.1	3.93	0.961

The actual pure component vapor pressure (P_i^{act}) was calculated using the DIPPR model where the equation and parameters are listed below for each component.

$$P_i^{act} = \exp\left(A + \frac{B}{T} + C\ln T + DT^E\right) \qquad (49)$$

Component	A	B	C	D	E	Min T (K)	Max T (K)
Water	7.36E+01	-7.26E+03	-7.30E+00	4.17E-06	2.00E+00	273.16	647.13
MEA	9.26E+01	-1.04E+04	-9.47E+00	1.90E-18	6.00E+00	283.65	678.2
PZ	7.05E+01	-7.91E+03	-6.65E+00	5.21E-18	6.00E+00	379.15	638

The resulting vapor pressures are given in Pa and the temperature inputs are in K. As evidenced

by Figure 23, the measured partial pressures of water compare very favorably to those predicted by the DIPPR model over this temperature range. The overall average error for the six data points was 3.6%, and when coupled with the fact that the accuracy of the FTIR is ± 2%, it appears these results validate our experimental method, and thus we should be able to proceed on to amine-water systems and be confident in the results.

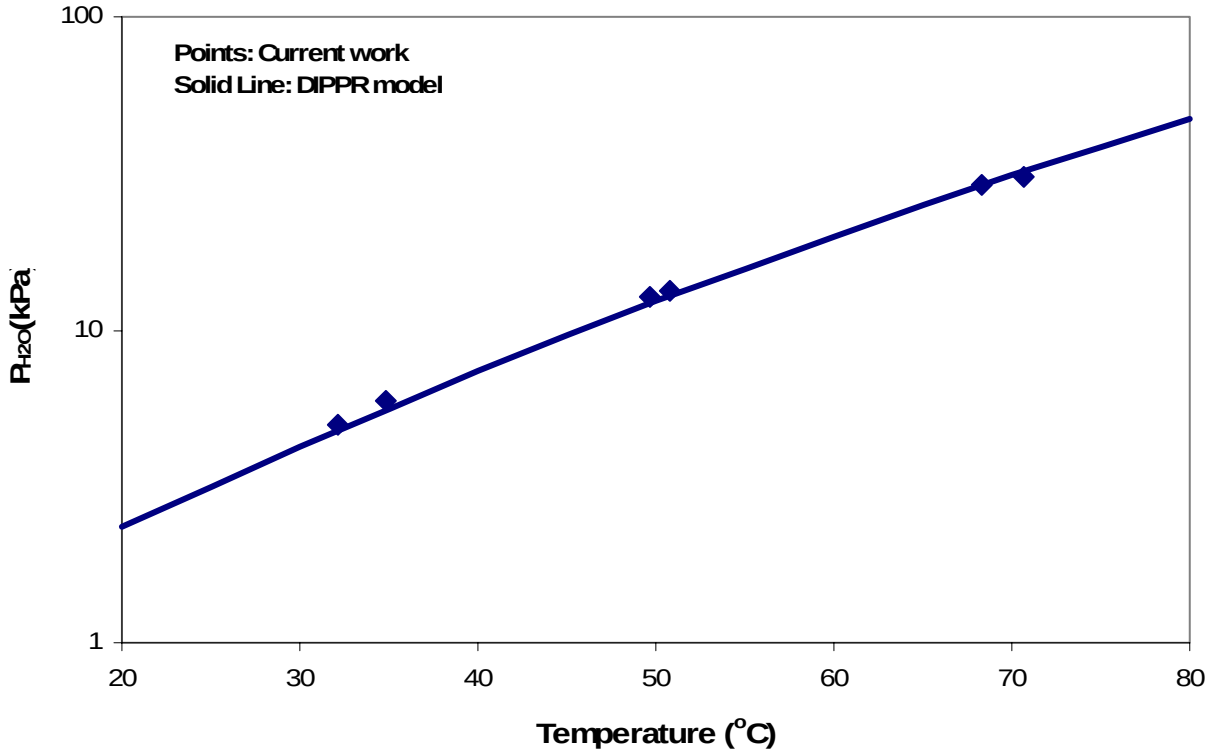

Figure 23: Experimental and predicted partial pressures of water as a function of temperature.

MEA-H_2O Results

The next system to be analyzed was a 7m MEA solution. The partial pressure results are shown in Figure 24 below. When compared to Posey's NRTL predictions, it is observed that the experimental partial pressure of water has less than 13% error, while the same binary interaction model severely under predicts the partial pressure of MEA at the given temperatures. This under prediction tends to suggest further research is needed in the modeling area to determine representative models for these binary amine-water solutions.

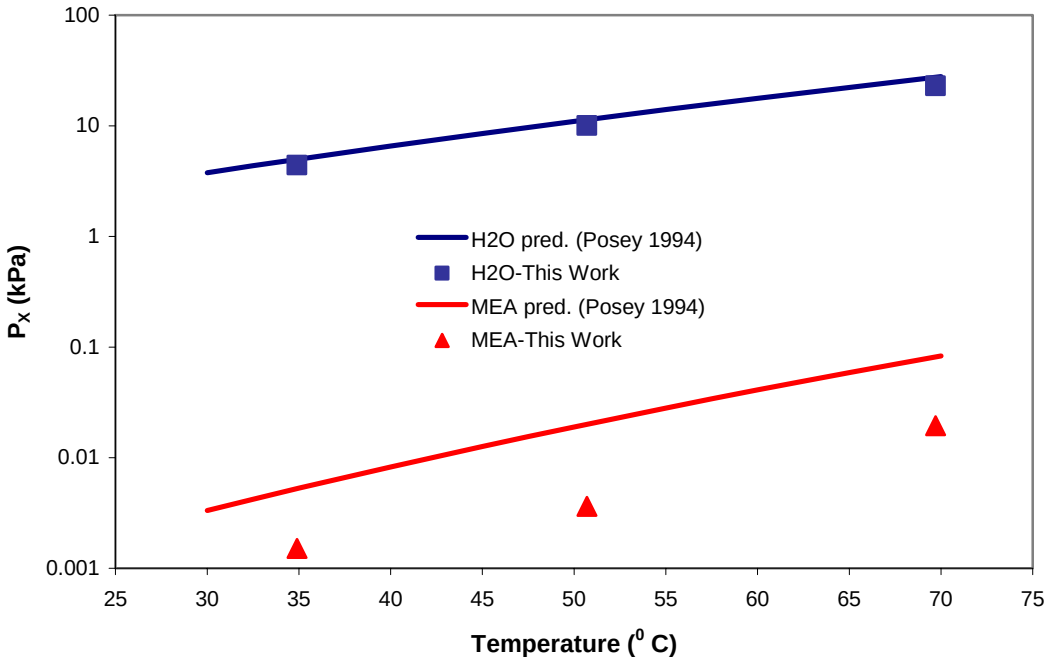

Figure 24. Experimental and predicted partial pressures of H_2O and MEA as a function of temperature.

The resulting partial pressure measurements were then used to calculate activity coefficients for both the water and MEA. The calculated activity coefficients were compared to those predicted by Posey's NRTL parameters in the Aspen software for 7m MEA at the given temperatures. The results are tabulated in Table 15.

Table 15. Experimental and predicted values of activity coefficients at different temperatures.

Temp (^{o}C)	P_{TOTAL} (kPa)	γ_{H2O}	γ_{MEA}	γ_{H2O}^{pred}	γ_{MEA}^{pred}
34.9	112.5	0.8847	0.1222	0.9948	0.4195
50.7	112.2	0.8853	0.0910	0.9988	0.4920
69.7	113.3	0.8432	0.1418	1.0026	0.5792

PZ-H_2O Results

The following section describes experimental results for the vapor phase speciation for 2.5 m PZ. Table 16 summarizes the range of experimental measurements.

Table 16. Summary of Low Temperature VLE Measurements for PZ Solutions.

Temp. (^{o}C)	P_{PZ} (kPa)	P_{H2O} (kPa)	Data Points
40 - 70	0.0003 - 0.0185	6.944 - 30.253	3

Figure 25 compares partial pressure measurements for H_2O and PZ based on Raoult's Law to predictions from the UNIFAC-DMD model for the 2.5 m PZ system from 40 – 70 ^oC. Experimental results for the partial pressure of H_2O differ by an absolute average deviation of 3.26% from model predictions, but model predictions for the partial pressure of PZ over predict the new experimental data from this study by ± 98%. This suggests that the UNIFAC-DMD group contribution model may not be accurately predicting the activity coefficient for PZ in aqueous solutions as shown in Table 17.

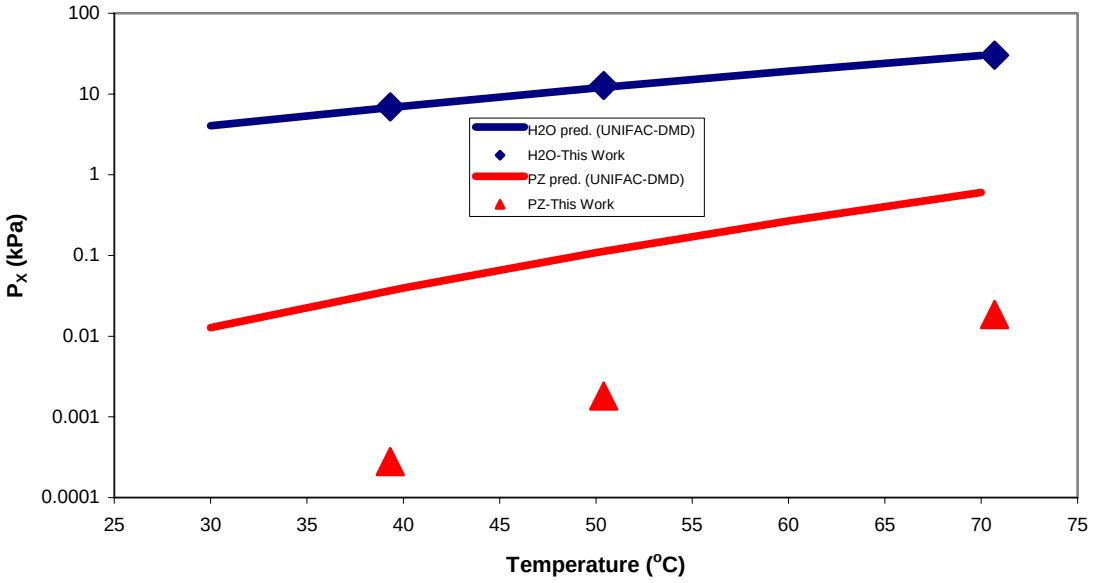

Figure 25. Comparison of experimental partial pressure of H_2O measurements to UNIFAC-DMD model predictions for the 2.5 m PZ system from 40-70 ^oC.

Table 17. Comparison of calculated activity coefficients of H2O and PZ from Raoult's Law to UNIFAC-DMD model predictions for the 2.5 m PZ system from 40-70 ^oC.

Temp (^oC)	TP (kPa)	γ_{H2O}	γ_{PZ}	γ_{H2O}^{pred}	γ_{PZ}^{pred}
39.3	112.0	1.0189	0.0052	1.0005	0.6885
50.4	119.8	1.0563	0.0186	1.0038	1.1669
70.7	120.0	0.9838	0.0707	1.0077	2.4219

Future Work

The FTIR will be used to measure PZ volatility in Campaign 4 at the pilot plant. Both the absorber inlet and outlet gas compositions are being measured and recorded via FTIR analysis and these results should give more activity coefficient data in loaded PZ solutions under industrial operating conditions. It is proposed that more research be aimed towards perfecting the model parameters used to predict partial pressures in the amine-water solutions, and more laboratory data collecting on these systems will ensure that these models shall become increasingly accurate as reliable data sets become available.

Task 5 – Corrosion

By Amorvadee (Amy) Veawab

Associate Professor, University of Regina

Supported by subcontract

Research objectives

The carbon dioxide absorption process using aqueous chemical solutions is subject to a number of operational difficulties, of which the most severe is corrosion of process equipment and solvent degradation. Corrosion problems have been receiving a great deal of attention because they have substantial impacts on the plant's economy, especially in terms of unplanned downtime, production losses, reduced equipment life, and extra-expenditure for restoring the corroded equipment and for treatment systems initiated to mitigate the corrosion. The corrosion problems also prevent the absorption process from achieving energy efficient operations.

The aqueous solution of blended potassium carbonate and piperazine has demonstrated to be a promising solvent for CO_2 capture from coal-fired power plant flue gas due to its capture performance and energy efficiency. It is our goal to further explore the promise of this solvent in an aspect of the potential operational problems. This project focuses on the investigation of corrosion of materials during CO_2 absorption and solvent regeneration in the presence and absence of solvent degradation products and chemical additives including oxidative inhibitors and corrosion inhibitors.

The research involves comprehensive literature review on the corrosion in CO_2 absorption process using potassium carbonate and piperazine, and experimental evaluations in the following sequences.

Task 1: Evaluation of corrosion in base solution (the blended potassium carbonate and piperazine) against the corrosion in an aqueous solution of monoethanolamine (MEA).

Task 2: Evaluation of corrosion in base solution containing degradation products.

Task 3: Evaluation of corrosion in base solution containing degradation products and oxidative inhibitors.

Task 4: Evaluation of inhibition performance of corrosion inhibitor in the presence of degradation products and oxidative inhibitors.

Results

Dr. Veawab has led the implementation of this research with a great assistance from one graduate student, Ms. Manjula Nairnar. Ms. Nainar has enrolled in our Master program in September 2005. She has a strong background in electrochemistry, which is extremely useful for corrosion experiments and analysis.

Over the past four months, we have completed the literature review of corrosion as given below. To date, the literature on corrosion in the CO_2 absorption process using an aqueous solution of blended potassium carbonate and piperazine has never been reported. As such, we

chose to review corrosion in the Benfield CO_2 absorption process using a hot-aqueous solution of potassium carbonate, which is the most relevant and speculated to behave similarly to the potassium carbonate-piperazine system.

Benfield process

The Benfield process uses a hot aqueous solution of potassium carbonate (K_2CO_3) for removing acid gases such as carbon dioxide (CO_2) and hydrogen sulfide (H_2S) from process gas streams (Bartoo et al., 1984). This process was initially developed by the U.S. Bureau of Mines, at Bruceton, Pennsylvania and the improvements to the process were made by Benson and Field in 1970s (Kohl and Nielson 1997). Since the reaction rate of CO_2 and potassium carbonate is slow, kinetic activators (e.g. diethanolamine (DEA)) are added to the solution.

The Benfield process is operated in a similar manner to a typical regenerative CO_2 absorption process. The feed gas containing acid gases enters the bottom of absorber and flows countercurrently to the potassium carbonate solution entering the top of absorber. As a result, acid gas absorption takes place. Below is an example of CO_2 absorption into potassium carbonate solution containing DEA kinetic activator where R_2NH, R_2NCOOH and $KHCO_3$ denote DEA and DEA carbamate and potassium bicarbonate, respectively.

$$R_2NH + CO_2 \rightarrow R_2NCOOH \quad (50)$$

$$R_2NCOOH + K_2CO_3 + H_2O \rightarrow 2KHCO_3 + R_2NH \quad (51)$$

$$K_2CO_3 + CO_2 + H_2O \leftrightarrow 2KHCO_3 \quad (52)$$

The rich solution containing absorbed acid gases is preheated and subsequently introduced to the regenerator where the acid gases are stripped by means of heat. The regenerated lean solution is cooled and sent back to the absorber for further gas absorption.

Corrosion problems and plant experiences

Corrosion generally causes substantial expenditure in addition to process costs. According to the CC Technologies & NACE International (Koch, 2001) in 1998, the plant expenditure due to corrosion in the United States was estimated at US$276 billions while that for petroleum refining alone was US$3.7 billion. Of this total, maintenance-related expenses are estimated at $1.8 billion, vessel turnaround expenses at $1.4 billion, and fouling costs are approximately $0.5 billion annually. This reflects a significant impact of corrosion problems in plant operations. In addition to the extra expenditure, corrosion also has an adverse impact on the safety of plant personnel. Often raised as a well-known event in the acid gas absorption plant history, an incident caused by severe corrosion occurred on July 23, 1984 (Mogul, M.G., 1999). A refinery at Romeoville, Illinois, owned and operated by the Union Oil Co. of California, experienced a disastrous explosion and fire. An absorber pressure vessel ruptured and released large quantities of flammable gases and vapors. Seventeen lives were lost, seventeen individuals were hospitalized, and more than US$100 million in damages resulted. All of these were caused by hydrogen-induced cracking and non-stress relieved repair welds. Even though no incidents as severe have been reported since, this incident is a serious indicator of the danger posed by the corrosion in an acid gas absorption unit.

The Benfield plants are known to be subject to severe corrosion. The potassium carbonate solution is corrosive to steel equipment. Dissolved CO_2 is the main contributor to such

corrosion. Pure carbonate solutions without dissolved CO_2 are not aggressive towards carbon steel. Table.18 summarizes plant experiences on corrosion problems in hot potassium carbonate systems. It is apparent that major types of corrosion found are general, pitting, erosion, stress corrosion cracking, and grooving type corrosion.

In addition to plant experiences, a number of research literature reported the severity of corrosion in the Benfield process. Beinstock et al. in 1961 revealed that a 40 wt% potassium carbonate solution saturated with CO_2 corroded carbon steel at the rate of 340 mils per year and the corrosion rate was considerably reduced in the presence of H_2S. Parkins et al. (1986) studied stress corrosion cracking in potassium carbonate systems. The results from a slow strain rate tests on C-Mn steel in a solution containing 300 g/L K_2CO_3 with CO_2 purging showed that stress corrosion cracking readily occurred in this system. The cracking domain was limited at the pH range of 8 to 11 and in the potential range of about -0.40 to -0.78 V. Another stress corrosion cracking study was conducted by Z.A. Foroulis (1987) on carbon steel using hot potassium carbonate/ bicarbonate solutions. It showed that this solution which contains CO_2 caused stress corrosion cracking of carbon steel in the presence of tensile stress. The data also indicated that stress corrosion cracking was only observed in the potential range of -0.85 to -0.55 V. (SCE) and at the free corrosion potential, similar to the results of Parkins et al. (1986). The cracking was predominantly transgranular at lower potentials and tended to be intergranular at higher potentials. It was also reported by Sutcliffe et al. (1972) that potassium carbonate solutions produced intergranular stress corrosion on carbon steel. Parkins et al. (1986) suggested that the stress corrosion cracking of carbon steels in carbonate solutions occurred by the dissolution process of metal at the crack tips**.** The dissolution rates at the crack tips were high enough to cause the crack walls to passivate, providing a large cathode inside the crack, coupled to a small anode at the crack tip where film rupture took place. G.McIntire et al. (1990) proposed the following reactions for iron dissolution in bicarbonate solutions.

$$Fe + 2H_2O \rightarrow Fe(OH)_2 + 2\,H^+ + 2e^- \quad (53)$$

$$Fe + HCO_3^- \rightarrow Fe(CO_3) + H^+ + 2e^- \quad (54)$$

$$Fe(OH)_2 + HCO_3^- \rightarrow Fe(CO_3) + H_2O + OH^- \quad (55)$$

$$FeCO_3 + HCO_3^- \rightarrow Fe(CO_3)^{2-} + H^+ \quad (56)$$

Table 18. Summary of plant experiences on corrosion in the Benfield process

References	Type of plant	Solvent	Acid gas	Corrosive area	Corrosion type	Reported causes
Johnson et al. (1987)	Oil and gas producing unit in USA	Hot Potassium Carbonate	CO_2 + H_2S	• Absorber • Process vessel	• Erosion • Pitting	• Increasing H_2S concentrations in the feed gas decreased the inhibiting effect of vanadium pentoxide (V_2O_5) • Galvanic attack
Piehl et al. (1986)	Ammonia plant in Netherlands	Hot Potassium Carbonate	-	• Bottom of absorber		
Cheravu et al. (1989)	Hydrogen plant in Kuwait	Hot potassium Carbonate	CO_2 + H_2S	• Absorber tower gas feed nozzle • Carbon steel circulating lines • Power Recovery Turbine	• Localized corrosion • Grooving type corrosion • Intergranular cracking	• Increasing CO_2 content in the feed gas • Decreasing strength of the vanadium pentoxide inhibitor in the solution • Suspended solids present in the liquid
Ferguson et al.(1991)	CO_2 plant at Texas	Hot potassium Carbonate	CO_2 + H_2S	• Absorber	• Localized corrosion • Pitting	• High H_2S concentration
Lele et al. (1992)	Ammonia plant in Bombay, India	Hot potassium Carbonate	CO_2	• Absorber	• N/A • Foaming	
Patel et al. (1996)	Ammonia plant in baroda, India	Potassium carbonate-arsenic oxide solution	CO_2	• Absorber	• Deep grooves • Fine cracks	• Lack of passivation because of semi lean and lean solutions

Bali et.al (1999)	Ammonia plant in Uttar Pradesh, India	Potassium carbonate-arsenic oxide solution	CO_2	• Regenerator • Vetrocoke absorber	• Erosion	• Increase in concentration of chemicals • The V+5/V ration was on the lower side.
Scott et al.	Ammonia plant in USA	Hot potassium carbonate and Catacarb catalyst	CO_2	• Bottom section of absorber	• Erosion • Stress corrosion cracking • Localized corrosion	• Carbonic acid attack on the walls • Lack of stress relief • High feed rates
Banks et al. (1967)	Ammonia Plant in Oklahoma	Hot potassium carbonate	CO_2	• 304 Stainless steel pumps and valves	• Erosion	• Due to high solution velocity and turbulence
Kolff (1986)	Ammonia Plant in Netherlands	Hot potassium carbonate	N/A	• Vessel wall behind Stainless steel linings	• Stress corrosion cracking	• Residual stresses

Factors affecting corrosion

Corrosion in carbonate system is affected by the following factors.

- concentration of carbonate and bicarbonate ion
- ratio of carbonate and bicarbonate
- temperature
- solution velocity

High carbonate concentration can cause corrosion damage to the system. Frolova et al. (1997) investigated the effect of bicarbonate ion concentration on corrosion rate of low and high strength steel in the 1 N sodium carbonate solutions. They reported that the corrosion rate increased with increasing bicarbonate concentration. The corrosion rate began to increase at 1 mg/L HCO_3^- and became twice as large at 100 mg/L. Banks et al. (1967) also revealed that high corrosion rate due to high bicarbonate concentration could not be easily reduced by introducing metavanadate corrosion inhibitor to the system. In addition to the total concentration of carbonates, a ratio of $K_2CO_3/KHCO_3$ plays a key role in corrosion rate. Lunarska et al. (1994) reported that minimum corrosion rate would be expected to occur at a $K_2CO_3/ KHCO_3$ ratio of about 0.1 – 0.2.

Temperature has a significant impact on corrosion. Frolova et al. (1997) reported that upon an increase in temperature from 20 to 80^oC, the corrosion rate increased twice in pure carbonate-bicarbonate solution, and by a factor of three to four in sulfide containing solutions. Increasing solution temperature from 75 to 96^oC led to increases in anodic current density of about an order of magnitude and a decrease in the extent of the passive region.

Solution velocity has a significant impact on corrosion. At high velocity, both erosion and velocity-dependent corrosion play an important role. Higher erosion is obtained due to the increasing force or shear stress exerted by the increasing solution velocity, turbulence and impingement of gas and solution on metal surfaces (Nielsen and Lewis, 1995). In case of the inhibited systems, a protective film is developed to cover the metal surface and suppress the excessive corrosion. However, this film can be removed or damaged by the shear force of a high velocity fluid stream. In the presence of solid contaminants such as iron carbonate, the solution velocity can cause even more severe erosion-corrosion (Meisen et al., 1996). In a system without a protective film, the corrosion rate is completely controlled by solution velocity (Videm and Dugstad, 1989). Raising the solution velocity reduces thickness of mass transfer film, allowing corrosive chemicals to reach the metal surface at a higher rate. Thus, if corrosion rate is controlled by the rate of mass convection through the film, corrosion is undoubtedly higher. This supports the report of Asperger (1994) that corrosion, not caused by erosion due to solids or cavitation, is a function of velocity.

Corrosion control

Materials:

It is known that carbon steel is prone to corrosion, and stainless steel (type- 304 and 316) is recommended for use in the plant locations subject to severe corrosion. According to a survey conducted in commercial plants using carbonate solutions, carbon steel is used generally for all equipment except at points of high liquid turbulence, such as letdown valve at the outlet of

absorber and the rotating elements of pumps. Straight carbon steel piping and gently curving elbows were suggested by Banks (1967) for handling hot carbonate solutions. However, carbon steel equipment with passivation layers is being used successfully ahead of stainless steel for handling the corrosive solution containing CO_2 at boiling temperatures (Bali et al., 1999). Benson and Field (1961) recommended 300 series of stainless steel such as 304 and 347 as it suffered negligible attack in 40 wt% potassium carbonate solution containing CO_2 and H_2S. Monel was also highly resistant to the attack in this mixture; its corrosion rate was 0.1 mils per year.

Corrosion problems in hot potassium carbonate system of a hydrogen plant was studied by Cheravu et al. (1989). Corrosion occurred in various places of the process equipment such as absorber gas feed nozzle, power recovery turbine, and carbon steel circulating lines. Change of carbon steel material to austenitic stainless steel 304L roll clad material for the gas nozzles was suggested to be a reliable long-term solution.

Banks (1967) tested a variety of steels in hot carbonate solutions. The results of their laboratory tests and plant experience indicated that the properly hardened type 316 stainless steel was neither corroded nor eroded by hot carbonate systems even at high velocity liquid impact solutions at a temperature of 127^{o}C and CO_2 pressure of 60 psig. Although type 304 stainless steel was not eroded by high velocity hot carbonate solution in laboratory tests, plant experience showed that it could fail when solution velocity and turbulence was high. Type 410 stainless steel was corroded by high velocity (100 ft/sec) carbonate systems. Bienstock et al. (1961) reported that epoxy cladding materials prevented corrosion and held up satisfactorily in the lab corrosion tests with boiling solutions of potassium carbonate saturated with CO_2 and H_2S. The material of cleats should be stainless steel (Bali, 1999).

According to Sorell (1990), the licensors of Benfield process specifically recommended that the following process equipment be made of 300 series of stainless steel.

- Solution circulating pumps
- Letdown hydraulic turbine
- Cladding and internals of regenerator shell above top bed (including top head)
- Top two type of packing in each bed
- All solution check valves, throttling valves and control valves
- Piping from rich solution letdown valve to regenerator
- Reboiler tubes, tube sheets, baffles and tie rods
- Acid gas separators, coolers and piping
- Overhead condensers
- Reflux pump and piping
- All demisters
- Cladding of feed gas separator

Stainless steel type 316 impellers, case rings and throat brushings were recommended in pumps handling potassium carbonate solutions as a safety measure (Buck and Leitch, 1958). In order to prevent the corrosion problems in process vessels using hot potassium carbonate solution, weld overlay with a continuously fused layer of stainless steel was reported to be the most attractive option in terms of cost and schedule. Because of the localized and high penetration rate of pitting corrosion, it was imperative that the finished stainless steel surface be

free of any defects such as cracks or pinholes which might allow contact of the process stream with underlying carbon-steel base metal. (Ferguson et al., 1991,1992e). New stainless steel (clad) columns or alternate processes were thought to be the most reliable, long term solutions to the corrosion problems in the hot potassium carbonate plants.

It was stated by Scott et al. that the hot potassium carbonate-CO_2 removal process, which was inhibited by pentavalent vanadium, could be operated successfully without corrosion, but sensitive to destabilizing upsets. Alloy strip lining could provide corrosion protection in areas where the inhibiting layer was broken. This however could lead to stress corrosion cracking in the steel behind the lining if the lining was penetrated by carbonate solution. Stainless weld overlay or cladding bonded directly to the steel should provide better protection with little or no risk of cracking.

Inhibitor:

Various inorganic chemicals were tested as potential corrosion inhibitors in boiling solutions of potassium carbonate saturated with acid gases (Bienstock and Field, 1961). Potassium chromate at 0.2% was very effective and could completely inhibit the corrosion of mild carbon steel and even galvanic couples of stainless steel and carbon steel in carbonate solution saturated with CO_2. In the presence of H_2S either with or without CO_2, the chromate ion was reduced, thus destroying its effectiveness as an inhibitor. Potassium dichromate (0.25-0.30 wt%) has been used as a corrosion inhibitor in a potassium carbonate plant in a petroleum refinery (Nikitina et al., 1984). Sodium metavanadate (0.1-0.2 wt%) eliminated corrosion of the steel disks in a 40 wt% solution of carbonate solution saturated with CO_2. N-alkyl trimethylene diamines at 0.02 – 0.50 wt% gave moderate protection, reducing the corrosion rate from 12 to 5-9 miles per year. These compounds were however effective only in the presence of H_2S.

Vanadation has been widely used for corrosion inhibition in the Benfield process. In spite of maintaining V^{+5} and V_2O_5 in the solution at required levels, the vanadation process begins only when the carbonate concentration is above 18-20 wt%. Proper vanadation can be recognized by a steady increase of V^{+4} in the solution at constant vanadium pentoxide levels. Vanadation is accelerated if a little amount of process gas is introduced in the system after the required carbonate levels are achieved.

The reaction for corrosion protection is:

$$V^{+5} + Fe^{+2} \rightarrow V^{+4} + Fe^{+3} \qquad (56)$$

In a gas plant in Texas (Johnson et al., 1987), the total vanadium was maintained above 1.4 wt% (as KVO_3) to maintain passivation, and pentavalent vanadium was maintained above 1.0 wt% (as V_2O_5). No measurable corrosion was observed with 1000 ppm vanadium (Eric Chen, 2004).

The Giammarco-Vetrocoke (GV) process in an ammonia plant in India also uses vanadium as a corrosion inhibitor. The hot potassium carbonate solution inhibited with vanadium can be operated safely. To maintain the electrochemical potential required for the protection of the passivation layer of metallic surfaces, it is necessary to keep 30 to 40% of the total vanadium in the pentavalent form and never be lower than 20% (Bali et al., 1999).

Patel et al. (1996) carried out an electrochemical evaluation of antimony corrosion inhibitor in GV solution on carbon steel. The results showed that the open circuit potential of carbon steel in the semi lean solution in the presence of 0.15% antimony oxide and 0.03% ferric ions shifted towards more noble values and stayed in the passive zone with an inhibition efficiency of 98.8%.

Corrosion inhibition of mild steel and stainless steel (type 304) by organic inhibitors including ATP and HEDP in the CO_2 absorption process was investigated by Sekine et al. (1990, 1992). The results suggested that 50 ppm ATP provided a good inhibition efficiency of 90% for mild steel. Mixed solutions containing (a) ATP-HEDP and (B) ATP-HEDP-DEA exerted a cooperative effect for inhibition. The highest efficiency was 92% in the solution containing 10 ppm ATP, 100 ppm HEDP and 3% DEA. For stainless steel type 304, the solution containing ATP under high pressure and temperature conditions was 95%. The inhibition efficiency of corrosion for mild steel in the test solution containing 200 ppm of HEDP under the atmospheric conditions was 80%. For stainless steel type 304, the inhibition performance of solution containing HEDP under high pressure and temperature conditions were 80 to 90%. HEDP also inhibited the scale formation. The inhibition mechanism for the organic inhibitors relied on adsorption. ATP molecule absorbs on the cathodic areas of the metal surface by creating a five-membered ring complex with metal. HEDP ion forms a six-membered ring complex with metal and absorbs on the anodic areas of the metal surface. When both ATP and HEDP are used, ATP and HEDP complementarily absorb on the metal surface, form a resistance film, and cooperatively inhibit the corrosion of metal.

A solution concentration beyond 30 wt% is highly vulnerable from the corrosion point of view. Less amount of $KHCO_3$ than K_2CO_3 is advantageous due to the vast difference in the solubility of $KHCO_3$ (60 grams/100 cc in boiling water) and K_2CO_3 (331 g/100 cc in boiling water). This will always maintain the bicarbonate in solution which would otherwise precipitate and start fouling the system. Foaming in the system may indicate not only silt and dust but also the presence of precipitated $KHCO_3$.

To minimize corrosion of Benfield plants, the inhibitor (KVO_3) content should be kept at a lower limit of 10 g/L. DEA should not be introduced while bringing the installation into operation, to promote the formation and growth of a stable protective layer. $KHCO_3$ concentration should be maintained at 1.0-1.5 M and the K_2CO_3/ $KHCO_3$ ratio at 0.2 –1.0 to minimize the possibility of passive layer degradation and corrosion. The optimum inhibitor content should be regularly adjusted accordingly to the carbonate concentration to provide reliable protection.

Johnson (1987) stated that the inhibiting effect of vanadium pentoxide could be reduced by changing process conditions including reduced circulation rates, changes in suppliers of vanadium, high column temperatures and contaminants. Increasing quantities of H_2S in the feed gas appeared to be the primary cause. Ferguson et al. (1991) reported that vanadium pentoxide could be used successfully as an inhibitor in the presence of low levels of H_2S. However, when the concentration of H_2S in the feed gas approached higher levels (100 – 1000 ppm, for example), the tendency of the H_2S to form an iron sulfide-iron pyrite scale competed with and effectively negated the protective scale forming abilities of the vanadium pentoxide inhibitor. The sulphide scales formed by the presence of H_2S were substantially less protective than the oxide scale and therefore subject the entire carbon-steel process system to pitting corrosive attacking areas where a premium scale could not be established.

Table 19. Corrosion inhibitors used in Benfield process

References	Company	Corrosion Inhibitor	Recommended concentration
Bali et al. (1999)	Ammonia plant in Uttar Pradesh, India.	Vanadium	0.5 wt % as V_2O_5
Patel et al. (1996)	Ammonia plant in Baroda, India	Combination of antimony oxide and ferric ions	0.15% antimony oxide and 0.03% ferric ion
Lunarska et al., (1994)	Benfield installation to purify gas.	Potassium vanadate.	10 g/L
Sekine et.al, (1992)	Experimental	2-Aminothiophenol (ATP) Mixed solutions of (a) ATP/HEDP (b) ATP/HEDP/DEA	ATP 50, 10 ppm HEDP-100ppm DEA – 3%
Sekine et al. (1990)	Experimental	HEDP	200 ppm
Johnson et al.(1987)	Gas plant at Texas	Vanadium Pentoxide	1.4 wt% -KVO_3 Pentavalent Vanadium – 1.0 wt %.
US patent 4116629	N/A	Nickel ions	10 ppm
Bienstock et al. 1961	Laboratory tests	Potassium dichromate Sodium metavanadate Vanadium pentoxide N-alkyl trimethylene diamines	0.2 wt% 0.2 wt % 0.15 wt % 0.02-0.5 wt%

References

Bali, V.K., Maheswari, A.K, "Case study of CO_2 removal system problems/failures in ammonia plant", *Ammonia Technical Manual*, 1999, 285-301.

Banks, W.P, "Corrosion in hot potassium carbonate system", *Mater. Prot.*, 1967, 9, 37.

Bienstock D., Field, J.H. "Corrosion Inhibitors for Hot-Carbonate Systems", *Corrosion*, 1961, 17(12), 87-90.

Bienstock D., Field, J.H., "Corrosion of Steels in Boiling Potassium Carbonate Saturated with Carbon Dioxide and Hydrogen Sulfide", *Corrosion*, 1961, 17(7), 89-91.

Chen, E, "Pilot plant for CO_2 capture using aqueous Piperazine/ Potassium Carbonate", *EPA Star Graduate Fellowship Conference*, 2004.

Cheravu, L., Sarraf, A.A., Baksh, H., "Corrosion problems in hot potassium carbonate system of a hydrogen plant", *Corrosion 89 conference*, paper no. 268.

Cullinane, J.T. "Thermodynamics and kinetics of aqueous piperazine with potassium carbonate for carbon dioxide absorption." Ph.D. Dissertation, Department of Chemical Engineering, The University of Texas at Austin, Austin, TX, 2005.

Dionex IonPac CS16 Analytical Column Product Manual. Revision 03. May 2003. http://www1.dionex.com/en-us/webdocs/manuals/ic/31747-03_CS16_V19.pdf (Accessed January 2005)

Ferguson, K.R., Stutheit, A.G., "Weld overlay chosen for corrosion repair at Texas CO_2 plant", *Oil & Gas Journal*, 1991, Dec, 54-57.

Ferguson, K.R, Stutheit, A.G., "Unusual weld overlay project stressed quality, safety", *Oil & Gas Journa*l, 1992, Jan, 69-74.

Ferguson, K.R., Stutheit, A.G., "Extensive testing ensures success of unusual weld-overlay project", 1992, Dec, 39-41.

Foroulis, Z.A, "Stress corrosion cracking of carbon steel in hot potassium carbonate/ bicarbonate solution", *Corrosion Engineering*, 1987, 36, 617-24.

Freguia, S. "Modeling of CO_2 removal from flue gases with monoethanolamine" M.S. Thesis, Department of Chemical Engineering, The University of Texas at Austin, Austin, TX, 2002.

Frolova L.V., Fokin, M.N., Zorina, V.E, "Corrosion – Electrochemical behavior of carbon steels in carbonate- bicarbonate solutions", *Protection of Metals*, 1997, 33(3), 249-252.

Gancy, A.B.; Durling, R.E., "Corrosion inhibition of stainless steel exposed to hot carbonates", United States Patent No. 4116629.

Gmehling, J., Li, J., Schiller, M., "A Modified UNIFAC Model. 2. Present Parameter Matrix and Results for Different Thermodynamic Properties", *Industrial & Engineering Chemistry Research*, 1993, 32(1), 178-93.

Goff, G.S., Rochelle, G.T., "Monoethanolamine Degradation: O_2 Mass Transfer Effects under CO_2 Capture Conditions", *Industrial & Engineering Chemistry Research*, 2004, 43(20), 6400-6408.

Johnson J., "Corrosion of a hot potassium carbonate CO_2 removal plant", *Corrosion 1987 Conference*, Paper no 189.

Jou, F.Y., Mather, A.E., "The solubility of CO_2 in a 30 mass percent monoethanolamine solution", *Canadian Journal of Chemical Engineering*, 1995, 73, 140-7.

Kohl, A.L., Nielsen, R.B., Gas Purification, 5th ed.; Gulf Publishing Company: Houston, Texas, 1997.

Leites, I.L., Berchenko, V.M., "Application of The Second Law of Thermodynamics for

Optimization of absorption Processes to Decrease the Energy Consumption", *Proc. International Conf. Energy Systems and Ecology*, 2003, 771-778.

Lele G.S., Ghate, P.H., Chakrayet, B.S., "Heavy corrosion problem in Benfield – CO_2 removal system of ammonia plant", 1992, 216-226.

Lunarska, E., Szyprowski, A., "Inhibitor protection and corrosion monitoring in Benfield installation to purify gas for synthesis", *British Corrosion Journal*, 1994, 29(3), 226-232.

McInire, G, Lippet, J., Yudelson, J., "The effect of dissolved CO_2 and O_2 on the corrosion of iron", *Corrosion*, 1990, 46(2), 91-95.

Might, J., Duquette, D.J., "Stress corrosion cracking of high-purity carbon steel in carbonate solutions", *Corrosion*, 1996, June, 428-434.

Nikitina A.K., Khvatkova V.P., Umnyashkina V.M., Cvershinina L.P., "Effect of inhibitors on corrosion rate of carbon steel in CO_2 saturated potassium carbonate solutions", *Chemistry and technology of fuels and oils (Historical Achieves)*, 1984, 20(8), 379-382.

Oyenekan, B.A., Rochelle, G.T., "Energy Performance of Stripper Configurations for CO_2 Capture by Aqueous Amines", Accepted for publication in the *Industrial & Engineering Chemistry Research Special Issue on CO_2 Capture*, October 13, 2005.

Parkins, R.N., Alexandridou, A., Majumdar, P., "Stress corrosion cracking of C-Mn steels in environments containing carbon dioxide", *Materials Performance*, 1986, 20-27.

Parkins, R.N., Belhimer, E., Blanchard, W.K., Jr, "Stress Corrosion Cracking Characteristics of a Range of Pipeline Steels in Carbonate-Bicarbonate Solution", *Corrosion*, 1993, 49, 951-966.

Patel, N.N., Pandya, M.M., Thanki, G.H., Mehta, M.H, "Evaluation of carbon steel corrosion in the CO_2 removal system of an ammonia plant", *Corrosion Prevention & Control*, 1996, 38-41.

Posey, M., Rochelle, G.T., "A Nonrandom Two-Liquid Model for Alkanolamine-Water Systems**,"** *Canadian Chemical Engineering Conference*, 1994.

Pouchert, C. J. *The Aldrich Library of NMR Spectra*. 2nd ed.; Aldrich Chemical Company: Milwaukee, WI, 1983.

Richard K. Bartoo, "Removing acid gases by Benfield process", *CEP*, 1984, 35-39.

Rochelle, G.T. "Innovative Stripper Configurations to Reduce the Energy Cost of CO_2 Capture" Prepared for the poster session at the Second Annual Carbon Sequestration Conference, Alexandria, VA, May 2003.

Rochelle, G. T. Personal Communication to Andrew Sexton. Austin, TX, 2005.

Scott, B., Daniels J.R., Chao, I., "Corrosion history of a hot pot CO_2 absorber", 127-133.

Sekine, I., Shimode, T., Yuasa, M., Takaoka, K., "Corrosion inhibition of structural steels in the CO2 absorption process by 1- (Hydroxyethylidene)-1, 1- diphophonic acid", *Industrial & Engineering Chemistry Research*, 1990, 29, 1460-1466.

Sekine, I., Shimode, T., Yuasa, M., Takaoka, K., "Corrosion inhibiton of structural steels in the CO_2 absorption process by 1- (Hydroxyethylidene)bis(phophonic acid), and Diethanolamine", *Industrial & Engineering Chemistry Research*, 1992, 31, 434-439.

Shoulders, B. Personal Communication to Andrew Sexton. Austin, TX, 2005.

Sorell, G., "Corrosion in natural gas processing plants", Topical Report May 1989-January 1990, prepared for Gas Research Institute (GRI), 1990, PB90- 205204.

Sutcliffe, J.M., Fessler R.R, Boyd W.K., Parkins R.N., "Stress corrosion cracking of carbon steel in carbonate solutions", *Corrosion*, 1972, 28(8), 313-320.

Wang, J. Personal Communication to Andrew Sexton. Austin, TX, 2005.